nature medicine

ARTICLES

https://doi.org/10.1038/s41591-021-01344-3

Check for updates

XCR1$^+$ type 1 conventional dendritic cells drive liver pathology in non-alcoholic steatohepatitis

Aleksandra Deczkowska[1,14]✉, Eyal David[1], Pierluigi Ramadori[2], Dominik Pfister[2], Michal Safran[3], Baoguo Li[1], Amir Giladi[1], Diego Adhemar Jaitin[1], Oren Barboy[1], Merav Cohen[1,4], Ido Yofe[1], Chamutal Gur[1,5], Shir Shlomi-Loubaton[1], Sandrine Henri[6], Yousuf Suhail[7], Mengjie Qiu[7], Shing Kam[2], Hila Hermon[8], Eylon Lahat[9], Gil Ben Yakov[3], Oranit Cohen-Ezra[3], Yana Davidov[3], Mariya Likhter[3], David Goitein[8,10], Susanne Roth[7], Achim Weber[11], Bernard Malissen[6,12], Assaf Weiner[1,15], Ziv Ben-Ari[3,10,15], Mathias Heikenwälder[2,15]✉, Eran Elinav[1,13,15]✉ and Ido Amit[1,15]✉

Non-alcoholic fatty liver disease (NAFLD) and non-alcoholic steatohepatitis (NASH) are prevalent liver conditions that underlie the development of life-threatening cirrhosis, liver failure and liver cancer. Chronic necro-inflammation is a critical factor in development of NASH, yet the cellular and molecular mechanisms of immune dysregulation in this disease are poorly understood. Here, using single-cell transcriptomic analysis, we comprehensively profiled the immune composition of the mouse liver during NASH. We identified a significant pathology-associated increase in hepatic conventional dendritic cells (cDCs) and further defined their source as NASH-induced boost in cycling of cDC progenitors in the bone marrow. Analysis of blood and liver from patients on the NAFLD/NASH spectrum showed that type 1 cDCs (cDC1) were more abundant and activated in disease. Sequencing of physically interacting cDC-T cell pairs from liver-draining lymph nodes revealed that cDCs in NASH promote inflammatory T cell reprogramming, previously associated with NASH worsening. Finally, depletion of cDC1 in XCR1^{DTA} mice or using anti-XCL1-blocking antibody attenuated liver pathology in NASH mouse models. Overall, our study provides a comprehensive characterization of cDC biology in NASH and identifies XCR1$^+$ cDC1 as an important driver of liver pathology.

NAFLD, a hepatic manifestation of metabolic syndrome, is present in 25% of the population globally. Up to 40% of individuals with NAFLD develop NASH, involving chronic inflammation and fibrosis associated with life-threatening cirrhosis and hepatocellular carcinoma, as well as non-liver-associated adverse outcomes such as type 2 diabetes and cardiovascular disease[1–3]. NAFLD/NASH has become the most common cause of chronic liver disease worldwide and will soon overtake hepatitis C virus as the leading cause of liver transplantation[1]. Mechanistically, NAFLD starts with progressive hepatic steatosis, manifested by the presence of enlarged lipid droplets in hepatocytes. Chronic fat overload induces endoplasmic reticulum stress, mitochondrial stress, aberrant hepatocyte metabolism and subsequent hepatocyte death, resulting in release of various danger signals, which trigger immune infiltration, lobular and portal inflammation, compensatory proliferation and in a chronic unresolved state, fibrosis[1,4]. Currently there is no efficient treatment to address NAFLD/NASH, except lifestyle modifications leading to weight reduction; a recommendation followed with little adherence[4,5].

The liver is the main organ responsible for metabolic and detoxification processes, but also acts as a frontline immune tissue. The liver is strategically positioned to interact with foreign antigens entering the body from the gut via the portal vein[6]. These include microbial products, toxins and food-derived antigens. To sense and respond to such complex stimuli in an appropriate manner, the liver is populated by a wide variety of immune cells and their composition changes significantly in response to infection or injury[7].

Systemic inflammation accompanying metabolic syndrome in general and hepatic immune composition in particular, was implicated in regulating different modalities of NAFLD and NASH. Mice lacking CD8$^+$ T cells are protected against multiple facets of metabolic syndrome, including development of NASH[8–13], while another study showed that type 2 immunity negatively affects the liver in NASH, despite its protective effects in the adipose tissue[14]. Triggering receptor expressed on myeloid cells 2 (TREM2)$^+$ macrophages accumulate in the liver with NAFLD[15,16] and NASH[17] and were suggested to limit liver damage in mice[18] but promote liver fibrosis in humans[19]. Although much progress has been made in

[1]Department of Immunology, Weizmann Institute of Science, Rehovot, Israel. [2]Division of Chronic Inflammation and Cancer, German Cancer Research Center Heidelberg (DKFZ), Heidelberg, Germany. [3]Liver Disease Center, Sheba Medical Center, Tel Hashomer, Israel. [4]Department of Clinical Microbiology and Immunology, Sackler Faculty of Medicine, Tel Aviv University, Tel Aviv, Israel. [5]Department of Medicine, Hadassah-Hebrew University Hospital, Jerusalem, Israel. [6]Centre d'Immunologie de Marseille-Luminy, Aix Marseille Université, INSERM, CNRS, Marseille, France. [7]Chirurgische Klinik, Allgemein, Viszeral und Transplantationschirurgie, Universitätsklinikum Heidelberg, Heidelberg, Germany. [8]Department of Surgery C, Sheba Medical Center, Tel Hashomer, Israel. [9]Department of Surgery B, Sheba Medical Center, Tel Hashomer, Israel. [10]Sackler School of Medicine, Tel Aviv University, Tel Aviv, Israel. [11]Department of Pathology and Molecular Pathology, University Hospital Zurich, Zurich, Switzerland. [12]Centre d'Immunophénomique, Aix Marseille Université, INSERM, CNRS, Marseille, France. [13]Division of Microbiome and Cancer, German Cancer Research Center Heidelberg (DKFZ), Heidelberg, Germany. [14]Present address: Departments of Immunology and Neuroscience, Institut Pasteur, Paris, France. [15]These authors contributed equally: Assaf Weiner, Ziv Ben-Ari, Mathias Heikenwälder, Eran Elinav, Ido Amit. ✉e-mail: aleksandra.deczkowska@pasteur.fr; m.heikenwaelder@dkfz-heidelberg.de; eran.elinav@weizmann.ac.il; ido.amit@weizmann.ac.il

identifying various immune mechanisms of NAFLD and NASH, these examples illustrate the complexity of liver immune composition and its stage-specific effect on liver pathology. Therefore, there is an urgent need to map immune cell heterogeneity of the liver and identify the mechanisms driving NAFLD/NASH-associated immune rearrangements to understand how we can best harness immune pathways to limit liver pathology.

Here we performed a comprehensive single-cell RNA sequencing (scRNA-seq) analysis of immune cells residing in the liver of healthy mice and in diet-induced NASH. Expansion of hepatic cDCs was found to be an early immune perturbation, present across various models of NASH, which occurs due to increased proliferation of cDC progenitors in the bone marrow. We further identified cDC1, to be elevated in livers and peripheral blood of patients with NAFLD/NASH. Genetic deletion of XCR1$^+$ cDC1 prevented NASH-associated changes in immune composition in the liver and liver damage, whereas partial blockade of cDC1 infiltration to the liver in advanced NASH attenuated disease symptoms. Sequencing of physically interacting cells (PIC-seq) defined signatures of DC–T cell interactions in liver-draining lymph nodes in healthy and NASH conditions and suggested activation of T cells as the mechanism driving cDC-dependent pathogenesis. Altogether, these findings point to a key negative role of cDC1 in metabolic liver disease and may have important implications for the development of effective immunotherapies for NASH.

Results

scRNA-seq of liver immune populations along NASH progression. To identify key immune players in NASH development and progression, we first used the model of methionine and choline-deficient diet (MCDD) feeding in mice, a model that faithfully recapitulates key features of human progression to NASH, including macrovesicular steatosis, ballooning, Mallory–Denk body formation, hepatocyte death and prominent immune infiltration (Extended Data Fig. 1a)[20,21]. Using scRNA-seq, we profiled CD45$^+$ immune cells from livers of mice after 0, 2, 4 and 8 weeks on MCDD, spanning the pathology from healthy state, through increasing steatosis and immune infiltration toward NASH (Fig. 1a and Extended Data Fig. 1b). Overall, our analysis included a total of 15,659 quality control-positive cells sampled from 12 mice at different time points (Extended Data Fig. 1c). We used the MetaCell algorithm[22] to divide cells into 173 coherent groups (metacells), classified them into 15 immune cell types (Fig. 1b) and annotated immune cell identities to each metacell on the basis of expression levels of most differentially expressed genes (Fig. 1c and Extended Data Fig. 2a). While mice fed a normal diet (ND) lacked significant changes in hepatic immune cell composition over time (Extended Data Fig. 2b–d), we observed a global reorganization of immune cell populations in the liver as early as day 14 on a NASH-inducing MCDD (Fig. 1d,e and Extended Data Fig. 2b–d). Prominent changes induced by MCDD in the immune compartment included a notable reduction in abundance of resident liver macrophages (Kupffer cells, KCs) and B cells and an increase in frequency of monocytes, macrophages and granulocytes, in line with previous reports[17,23–32].

Unexpectedly, the most prominent change in the immune compartment in the NASH condition was observed among cDCs (Fig. 1d,e and Extended Data Fig. 2b–d). Specifically, cDC1 cells (expressing *Itgae*, *Naaa*, *Xcr1* and *Clelc9a*) and cDC2 cells (expressing *Sirpa* and *Cd209*), as well as migratory (or mature) DCs (mDCs; expressing *Ccr7*, *Tspan3*, *Tmem123*, *Cd40*, *Cd83* and *Cd86*) were expanded up to fourfold, as early as 2 weeks following MCDD (Fig. 1d,e and Extended Data Fig. 2b–d). Under physiological conditions, as well as in the case of damage or infection, cDCs integrate information about the immune environment in tissues (including antigens and surface-bound and soluble stimulatory and inhibitory signals) to instruct T cell differentiation in draining lymphoid organs[33]. As the role of cDCs in metabolic liver pathology development and progression has not been comprehensively studied so far, we decided to investigate the role of cDCs in NASH.

Hepatic cDC subsets across the NAFLD/NASH spectrum. We first confirmed the increased numbers of cDCs in the livers of mice fed an MCDD for 2 weeks using fluorescence activated cell sorting (FACS) and standard cDC markers, where cDCs were defined as CD45$^+$Lin$^-$ (CD3, CD19, B220, Ly6g, Ly6c, NK1.1 and Ter119) MHC-II$^+$CD11c$^+$ (Extended Data Fig. 3a). As cDC are a heterogeneous cell type and their markers may vary across tissues[33] we used scRNA-seq analysis of index-sorted cDCs from Xcr1$^{Cre\text{-}mTFP1}$ (cDC1 reporter) mice to confirm the use of this gating strategy to define cDCs with high precision (Extended Data Fig. 3b). FACS analysis confirmed elevated frequency of cDCs among CD45$^+$ liver cells in MCDD (Fig. 2a and Extended Data Fig. 3c). As dissociation of liver tissue into a single-cell suspension is known to pose technical challenges, which may result in disproportional isolation of some cell types over others[34], we quantified cells expressing cDC markers CD11c and MHC-II in mouse livers using immunohistochemistry (IHC). This analysis confirmed a marked elevation of double-positive MHC-II$^+$CD11c$^+$ cells in the livers of MCDD-fed mice (Fig. 2b,c and Extended Data Fig. 3d).

To determine whether the observed increased numbers of cDCs was an MCDD-specific effect, we next analyzed cDC numbers in other murine models metabolically challenging the liver. Multiple studies showed that consumption of a western diet, containing high trans-fats (WD) and choline-deficient, high-fat diet (CDHFD) induces a slowly progressing liver pathology similar to human NAFLD, which ultimately leads to NASH, while recapitulating insulin resistance and a milder form of liver inflammation compared to the MCD dietary model[10,12] (Extended Data Fig. 3e–g). In both WD and CDHFD, we observed an increased frequency of Lin$^-$MHC-II$^+$CD11c$^+$ cDCs among CD45$^+$ cells in the liver when compared to age-matched, ND-fed controls (Fig. 2d,e and Extended Data Fig. 3f) in agreement with recent reports[31]. High-fat diet (HFD) feeding and deficiency in leptin (*Ob/Ob* mice) or leptin receptor (*Db/Db* mice) are associated with obesity and metabolic syndrome and are known to induce hepatic steatosis but lack liver damage and necro-inflammation typically found in NASH (Extended Data Fig. 4a)[21,35–37]. After 6 months of feeding with an HFD, 12-week-old *Db/Db* mice and 9-week-old *Ob/Ob* mice also showed increased levels of hepatic cDCs (Extended Data Fig. 4b).

We next set off to investigate in detail the DC subsets present in healthy and NASH livers. Tissue-resident cDCs include two main subsets: cDC1 and cDC2. cDC1 cells are defined by surface expression of CD103 (*Itgae*) and XCR1 in mice and their ability to cross-present cell-associated antigens to CD8$^+$ T cells and induction of cytotoxic T cell responses, which is critical for protection against viruses and neoplasia. The cDC2 cell subset is a heterogeneous population, marked by surface expression of CD172α (*Sirpa*) (in mice). cDC2 cells share some molecular characteristics with macrophages, for example expression of CD11b (*Itgam*) and are thought to be involved in priming CD4$^+$ T cells. mDCs are rare in peripheral organs and express co-stimulatory and co-inhibitory molecules (such as *Cd40* and *Cd86*) and trafficking molecules (such as *Ccr7*), which direct them to secondary lymphoid organs for antigen presentation to T cells[38].

To test whether NASH is associated with elevated frequencies of hepatic cDC1, cDC2 and mDCs, as observed in scRNA-seq (Fig. 1) we applied flow cytometry analysis with standard markers; CD45$^+$Lin$^-$ MHC-II$^+$CD11c$^+$ for cDCs, which were further separated into CD103$^+$CD11b$^-$ cDC1 cells, CD103$^-$CD11b$^+$ cDC2 cells (ref. [33]) and CCR7$^+$ or CD86$^+$ mDCs (Extended Data Fig. 3a). Combination of scRNA-seq with surface staining of cDCs confirmed that FACS-based quantifications using this gating strategy is

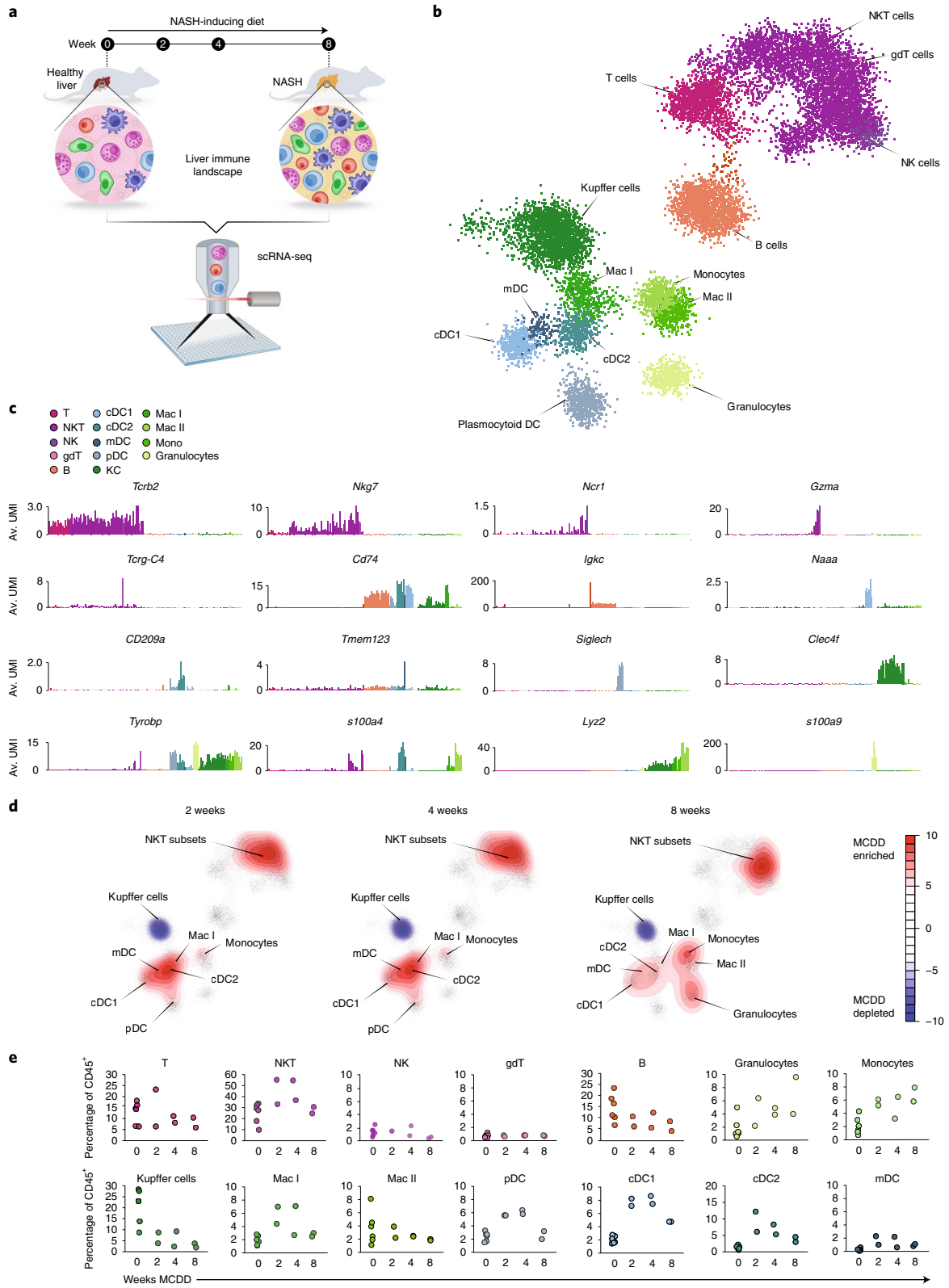

Fig. 1 | scRNA-seq characterization of the liver immune niche during development of NASH. a, Schematic of the experimental approach. Immune cells from livers of mice kept on a NASH-inducing MCDD for 2, 4 and 8 weeks were isolated and analyzed using scRNA-seq. **b**, k-nearest neighbors (k-NN) graph of 15,659 quality control (QC)-positive immune cells (173 metacells) from livers of 12 mice fed an ND or MCDD. gdT, gamma-delta T cells. **c**, Average (Av.) unique molecular identifier (UMI) count of selected genes across metacells. **d**, Density plots depicting enrichment analysis of MCDD as compared to ND, showing cell type abundance changes at 2, 4 and 8-week time points projected on the k-NN graph. Red areas represent enrichment and blue areas represent depletion. **e**, Plot showing percentage of ND or MCDD (at 2, 4 or 8 weeks) cells out of total CD45$^+$ cells in each of the clusters identified in **b**. Each data point represents an individual animal.

robust and precise (Extended Data Fig. 3b). We observed elevated frequencies of both cDC1 and cDC2 cells among CD45$^+$ cells in the livers of mice kept on an MCDD for 2 weeks (Fig. 2f and Extended Data Fig. 4c) as well as mice fed a WD or CDHFD for 6 months (Fig. 2g,h). We further quantified cDC1 cells directly in liver sections. Imaging of livers of mice kept on an MCDD for 2 weeks and mice fed a CDHFD for 6 months (as well as their ND-fed counterparts) confirmed elevated numbers of cDC1 cells in the NASH condition (Fig. 2i–l and Extended Data Fig. 4d,e). Similarly, our analysis revealed an elevated percentage of mDCs among cDCs as well as CD45$^+$ immune cells in NASH livers in all three dietary models (Fig. 2m–o and Extended Data Fig. 4f). Analogous analysis in livers of HFD, *Db/Db* and *Ob/Ob* mice revealed elevation of the cDC2 subset, whereas cDC1 populations did not increase in either of these obesity models (Extended Data Fig. 4g,h). These results suggested that non-inflammatory accumulation of lipids in hepatocytes associated with HFD-, *Db/Db*- or *Ob/Ob*-induced obesity and NAFLD may coincide with increased numbers of cDC2 cells in the liver, whereas increased frequencies of cDC1 cells co-occur with liver damage associated with inflammation.

To test whether the pathological environment of the NASH liver modulates cDC phenotypes, we compared gene expression between MCDD and ND conditions within cells annotated as cDC1, cDC2 or mDC and found only minor diet-dependent changes, primarily indicating enhanced maturation in cDC1 cells (*Tmem123* and *Ccl5*) and antigen presentation in mDCs (*Ha-Aa* and *Cd74*) (Fig. 2p). This analysis suggested that unlike macrophages, which are strongly impacted by tissue signaling environments[32,39], DCs alter their developmentally preset phenotypes to a much lesser extent[33]. Rather, increased DC numbers in the liver and the enhanced maturation signature reflected by expression of co-stimulatory and migratory molecules amplify basic cDC functions related to migration to the draining lymph nodes and antigen presentation to T cells.

Hepatic cDC in human NASH. We next investigated DCs in human NAFLD and NASH. A recent study reported that cDC-related gene expression signatures in human livers correlated to NASH pathology[30], suggesting that increased cDC infiltration is also a hallmark of human NASH. To investigate this observation in greater detail, we isolated CD45$^+$LIN$^-$CD11C$^+$ cells from liver biopsies of patients undergoing bariatric surgery. Liver pathology in these samples was evaluated based on NAFLD activation score (NAS); a standard pathology score combining grading of lobular inflammation, steatosis and ballooning in hematoxylin and eosin (H&E) staining[40]. Samples scoring low (NAS = 0 or 1) were considered as 'healthy' and samples scoring high (NAS = 4–6) were labeled as 'NASH'. Sorted and sequenced CD45$^+$LIN$^-$CD11C$^+$ cells were divided into coherent groups using the metacell pipeline[22] and annotated based on gene expression differences (Fig. 3a,b and Extended Data Fig. 5a–e). Specifically, transcriptomic, surface marker and functional analyses have concluded that CD1c$^-$CD141$^+$XCR1$^+$ DCs in humans correspond to murine cDC1 cells, whereas human CD1C$^+$CD141$^-$ cells are equivalent to cDC2 cells in mice[41] (Fig. 3a and Extended Data Fig. 5d). In both populations NASH-associated changes suggested increased activation toward antigen presentation, reflected by elevated expression of maturation markers *LAMP1* and *LAMP3* and chemokines *CCL22* and *CCL17* in cDC2 cells and downregulation of *SOCS1* in cDC1 cells (Fig. 3b). As our previous investigation in mouse models suggested that expansion of cDC2 cells accompanies simple steatosis and excess cDC1 cells are specifically related to NASH, we quantified CD141$^+$ cDC1 cells in healthy and NASH liver biopsies and found a NASH-dependent elevation in CD141$^+$ cells (Fig. 3c,d). Correlation analysis revealed a positive association between liver cDC1 cell numbers and NASH pathology hallmarks, such as NAS, its individual components and serum activity of alanine aminotransferase (ALT) and aspartate aminotransferase (AST), which are standard indicators of liver and systemic injury, respectively (Fig. 3e). Moreover, analysis of cDC subtype frequency in the blood of patients with NAFLD and NASH, further demonstrated that elevated numbers of cDC1 cells are associated with liver pathology (Fig.3f–i and Extended Data Fig. 5f).

Enhanced proliferation of cDC progenitors in NASH. We next investigated the source of excess cDCs in NASH. Both under physiological conditions and in physiological stress, such as infection or tissue damage, the half-life of DCs in tissues spans only a few days. The local DC pool is constantly replenished from bone-marrow-derived precursors[38]. Recent studies have unraveled that various paradigms of homeostasis disruption, such as infection and cancer, psychosocial stress, insufficient sleep, as well as pathways related to metabolic syndrome, such as hyperlipidemia, obesity and exercise shape hematopoiesis output[42]. Therefore, we asked whether liver damage associated with NASH modulates generation of new DC precursors in the bone marrow. Under physiological conditions, DCs originate from a branch of myeloid hematopoiesis cascade via the monocyte-DC progenitors (MDP), common DC progenitors (CDPs) and cDC1 and cDC2 precursors (pre-DC1 and pre-DC2, respectively), which migrate from the bone marrow into the blood and seed peripheral tissues to differentiate locally into cDC1 and cDC2[33,43]. To test whether NASH modulated the cDC-committed hematopoietic lineage we investigated CDPs in bone marrow and pre-DCs in bone marrow, liver and blood of ND- and MCDD-fed mice.

We first focused on tracing the rate of proliferation in cDC progenitors. We injected 5-bromodeoxyuridine (BrdU), a

Fig. 2 | NASH-induced increase in conventional dendritic cell subtypes. a, Percentage of cDCs among CD45$^+$ cells in the livers of mice fed ND or MCDD for 2 weeks, based on FACS data ($n = 5$ mice per group). **b**, Immunofluorescence images of CD11c (red), MHC-II (green) and CD31 (vasculature marker; magenta) in liver sections of mice fed an ND or MCDD for 2 weeks. Cell nuclei are stained with 4,6-diamidino-2-phenylindole (DAPI) (blue). Scale bar, 30 µm. Images are representative of two independent experiments. **c**, Quantification of MHC-II$^+$CD11c$^+$ cells from 3–4 randomly selected liver areas per animal as shown in **b** ($n = 4$ ND and 3 MCDD mice per group). **d**,**e**, Percentage of cDCs among CD45$^+$ cells in livers of mice fed an ND or WD for 6 months (**d**) or CDHFD for 6 months (**e**), $n = 6$ mice per group. **f**–**h**, Percentage of cDC1 and cDC2 among CD45$^+$ immune cells in livers of mice fed an ND or MCDD for 2 weeks, $n = 3$ mice per group (**f**), WD for 6 months, $n = 3$ mice per group (**g**) or CDHFD for 6 months, $n = 6$ mice per group (**h**), based on FACS quantification. **i**,**j**, Representative immunofluorescence images (**i**) and quantification (**j**) of XCR1$^+$ (red), CD11c$^+$ (magenta), MHC-II$^+$ (green) and DAPI$^+$ (nuclear stain, blue) cells in liver sections of mice fed an ND or MCDD for 2 weeks. For quantification, 3–4 randomly selected fields per mouse were averaged ($n = 3$ independent animals per group). Scale bar, 30 µm. Images are representative of two independent experiments. **k**,**l**, Representative immunofluorescence images (**k**) and quantification (**l**) of CD103$^+$ (white) CD11c$^+$ (red), MHC-II$^+$ (green) and DAPI$^+$ (nuclear stain, blue) cells in liver sections of mice fed an ND or CDHFD for 6 months. Scale bar, 50 µm. Images are representative of two independent experiments. For quantification, 5–10 randomly selected fields per mouse were averaged ($n = 6$ ND and 7 CDHFD mice). **m**–**o**, Percentage of mDCs among CD45$^+$ cells and cDC gate in livers of mice fed an ND or MCDD for 2 weeks, $n = 3$ mice per group (**m**), WD for 6 months $n = 6$ animals per group (**n**) or CDHFD, $n = 6$ animals per group (**o**) based on FACS quantification. In all graphs data are presented as mean ± s.e.m. *P* values were determined by two-tailed Student's *t*-test; $^{***}P < 0.001$, $^{****}P < 0.0001$. **p**, Scatter-plot comparing gene expression levels in hepatic cDC1, cDC2 and mDCs in ND-fed (*x* axis) and MCDD-fed mice (*y* axis) ($\log_2$ scale, Mann–Whitney *U*-test).

DNA-intercalating agent, to mice that had been kept on an ND or MCDD for 2 weeks and quantified BrdU incorporation 10 h after injection in CDPs and pre-DCs in the bone marrow. We defined cDC-committed CDPs and pre-DCs by FACS markers; CDPs were defined as Lin$^-$CD135$^+$CSF$^-$1R$^+$CD117^{int} and pre-DCs as Lin$^-$CD172α$^-$CD11c$^+$CD135$^+$ (Extended Data Fig. 6a)[43,44]. While MDP were highly proliferative in both groups (Extended Data Fig. 6b), we found a significant increase in frequency of BrdU$^+$ cells within bone marrow CDPs and pre-DCs of mice fed an MCDD for 2 weeks, demonstrating that MCDD-induced liver damage promotes increased proliferation of DC-committed progenitors (Fig. 4a). We further observed that frequencies of circulating pre-DCs in the blood were also significantly increased in the MCDD condition (Fig. 4b). Finally, percentages of BrdU$^+$ cells among DCs and

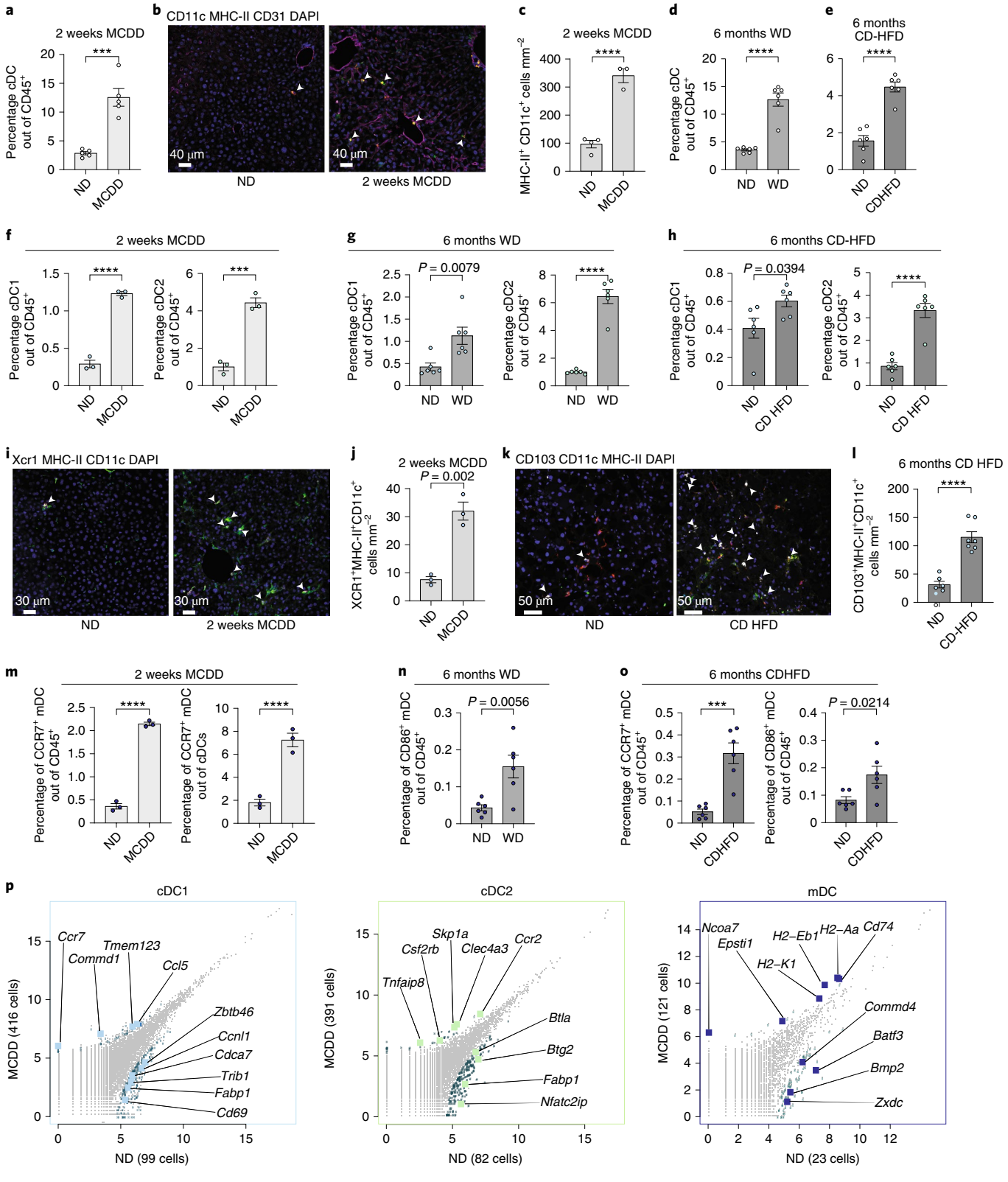

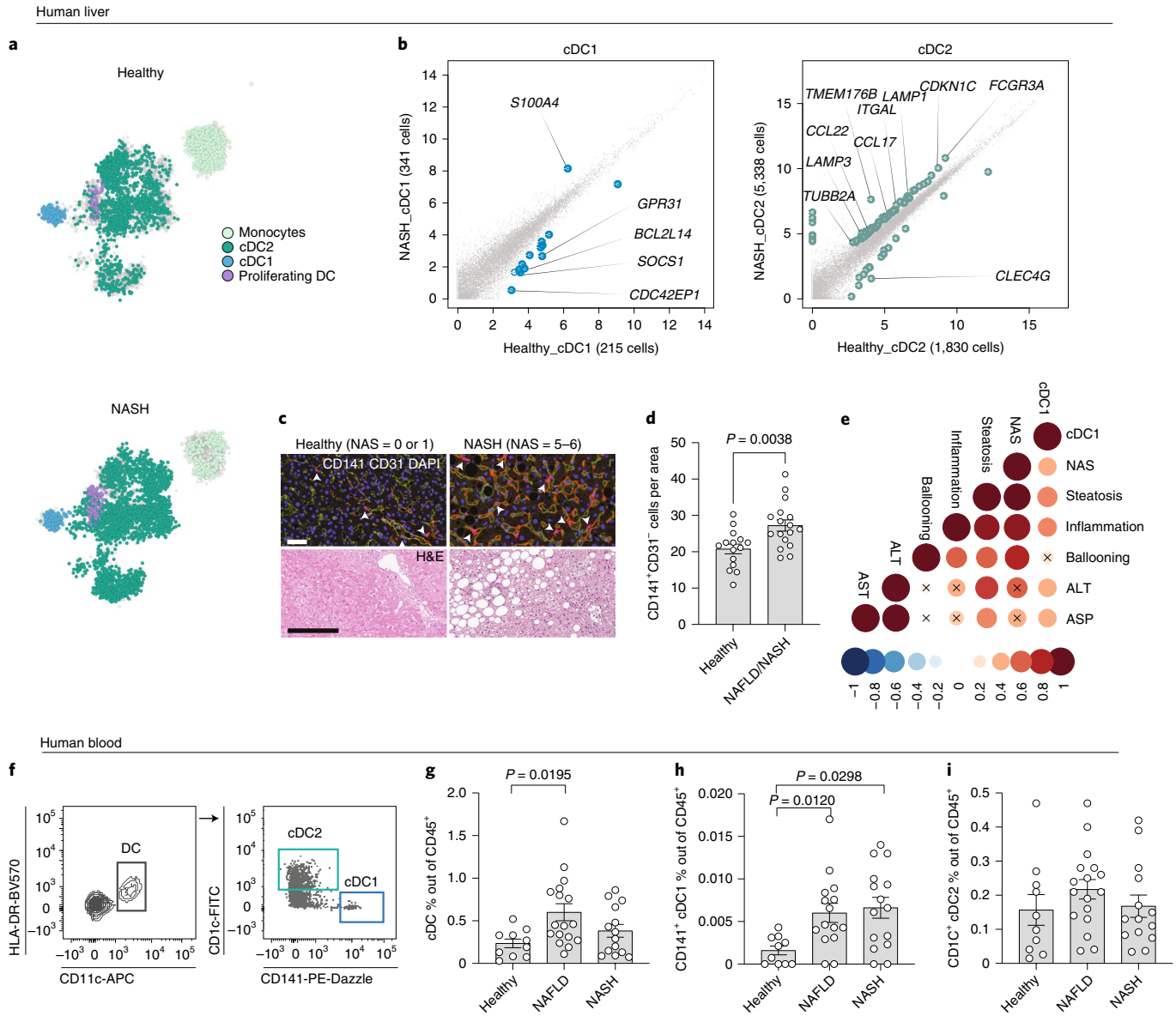

Fig. 3 | cDCs in human NASH. a, k-NN graph of QC-positive CD45$^+$Lin$^-$CD11c$^+$ cells from liver biopsies of healthy patients (NAS = 0 or 1) and patients with NASH (NAS ≥ 4). **b**, Scatter-plot comparing gene expression levels in hepatic cDC1 and cDC2 cells in healthy patients (*x* axis) and those with NASH (*y* axis) ($\log_2$ scale, Mann–Whitney *U*-test). **c**,**d**, Representative H&E staining and immunofluorescence images (**c**) and quantification (**d**) of CD141$^+$ (red), CD31$^-$ (green) and DAPI$^+$ (nuclear stain, blue) cDC1 cells in sections of healthy and NASH livers. Scale bar, 50 µm (top) and 200 µm (bottom). Images are representative of two experiments. For quantification, 5–10 randomly selected fields per patient were averaged ($n = 15$ patients with healthy livers and 17 patients with NAFLD/NASH). **e**, Correlation analysis between CD141$^+$CD31$^-$ cDC1 cell count and NASH pathology parameters in human livers across the NASH pathology spectrum ($n = 32$ patients; two-tailed Spearman correlation; crossed-out points $P > 0.01$; color and circle size indicate R^2). **f**, representative flow cytometry contour plots of cDCs, cDC1 and cDC2 cell selection out of CD45$^+$CD14$^-$CD19$^-$ gate in human blood. **g**–**i**, Percentage of CD11c$^+$HDL-DR$^+$ cDCs (**g**), CD141$^+$CD1c$^-$ cDC1 cells (**h**) and CD141$^-$CD1c$^+$ cDC2 cells (**i**) among CD45$^+$ immune cells in the blood of patients with NAFLD and NASH as well as healthy individuals ($n = 10$ healthy, 15 with NAFLD and 15 with NASH). In all graphs data are presented as mean ± s.e.m.; two-tailed Student's *t*-test or one-way analysis of variance (ANOVA) with Tukey's multiple comparisons test.

immature pre-DC among CD45$^+$ immune cells in the liver were also increased in MCDD-fed mice (Fig. 4c,d). Altogether, these results highlight that NASH-induced liver damage promotes activity of the DC-committed branch of hematopoiesis in bone marrow.

To better understand this process, we performed scRNA-seq of sorted CDPs from bone marrow and pre-DCs from bone marrow, blood and liver of mice kept on ND or fed an MCDD for 2 weeks. We analyzed 9,256 quality control-positive cells, which were grouped based on similarity using the metacell algorithm (Extended Data Fig. 6c) and annotated these on the basis of expression of marker genes (Extended Data Fig. 6d)[43]. Cells classified as MDPs, CDPs, pre-DCs or DCs were ordered according to their gene expression (Fig. 4e and Extended Data Fig. 6d,e). Analysis of the cell cycle signature for each metacell revealed elevated frequency of cycling cells among pre-DCs in blood of MCDD-fed mice compared to mice kept on an ND (Fig. 4f) in accordance with our BrdU analysis. Altogether, analysis of the bone marrow, blood and liver in an MCDD-based NASH mouse model showed that

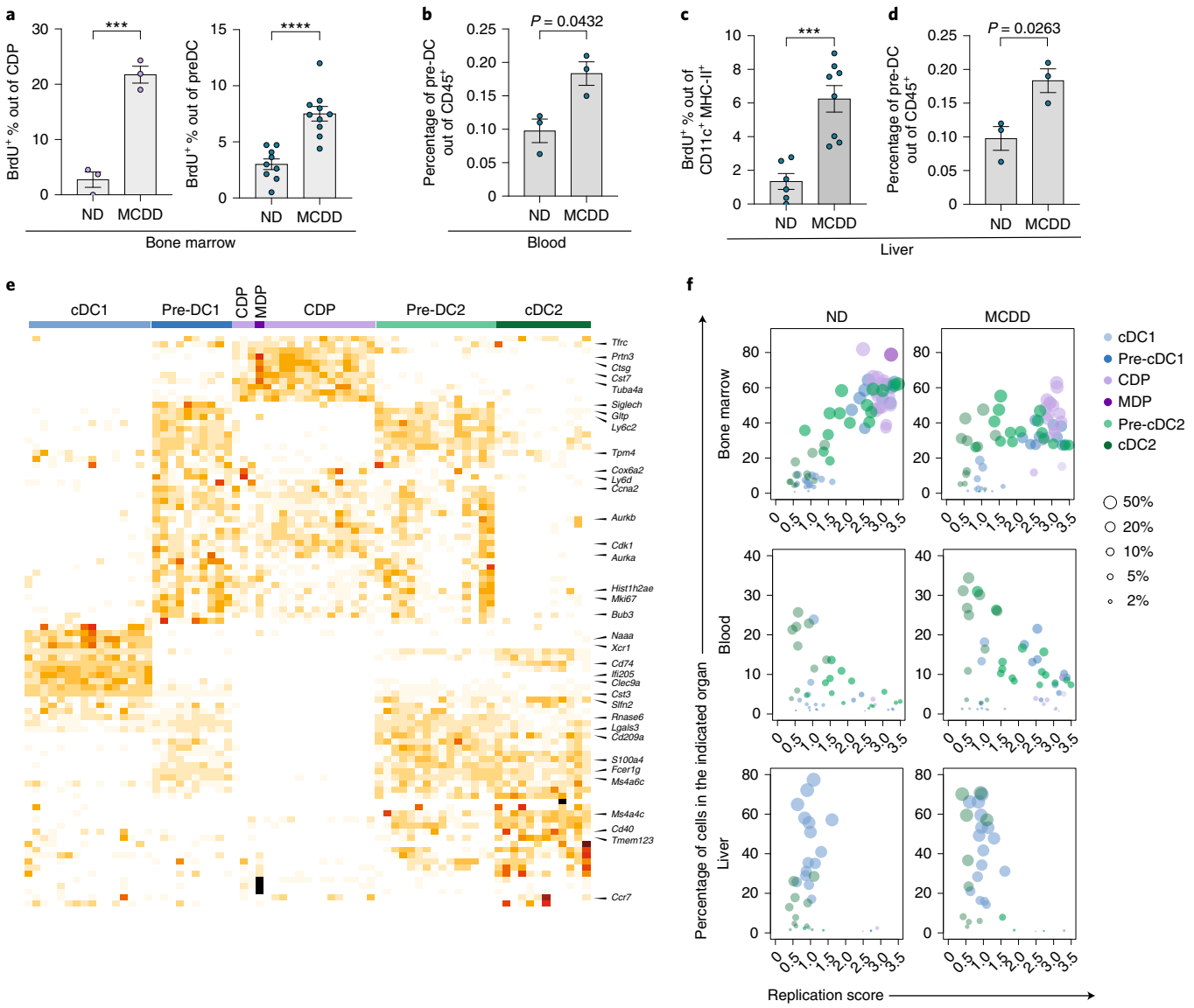

Fig. 4 | NASH boosts DC-poiesis output in bone marrow. a–d, Quantification of BrdU$^+$ cells among CDPs ($n=3$ mice per group) and pre-DCs ($n=9$ ND mice and 10 MCDD mice) in bone marrow (**a**), pre-DCs in blood ($n=3$ mice per group) (**b**), BrdU$^+$ cells among CD11c$^+$MHC-II$^+$ cDCs ($n=6$ ND and 8 MCDD mice) (**c**) and pre-DCs among CD45$^+$ cells in the liver ($n=3$ mice per group) (**d**) in mice fed an ND or MCDD for 2 weeks based of FACS analysis. Data are presented as mean ± s.e.m. *P* values were determined by two-tailed Student's *t*-test, $^{***}P<0.001$, $^{****}P<0.0001$. **e**, Heat map illustrating expression of DC maturation markers in DC lineage-related metacells in single MDPs and CDPs from bone marrow and pre-cDCs and cDCs, isolated from liver, bone marrow and blood of wild-type mice fed an ND or MCDD for 2 weeks. **f**, Scatter-plot showing replication score and representation in each organ analyzed. Each circle represents a metacell of MDPs, CDPs, pre-DCs or DCs in bone marrow, blood and liver, comparing ND and MCDD conditions.

excessive liver cDCs are derived from increased proliferation of cDC progenitors.

Altered T cell priming in liver lymph nodes in NASH. We next sought to determine the molecular function of cDCs in NASH. As gene expression analysis of hepatic cDCs in NASH livers revealed signatures related to increased migration and antigen presentation and T cell activation was previously implicated in NASH worsening in mice and humans[9,10,12,13,30], we investigated molecular signatures of DC–T cell pairs in liver-draining lymph nodes in the MCDD model of NASH. To this end we excised portal and celiac lymph nodes from mice kept on an MCDD or ND for 2 weeks[45]. After mild digestion, single DCs (CD45$^+$Lin$^-$MHC-II$^+$ CD11c$^+$), single T cells (CD45$^+$Lin$^-$TCR-β$^+$) as well as physically interacting DC–T cell pairs (CD45$^+$Lin$^-$MHC-II$^+$CD11c$^+$TCR-β$^+$; 'PICs') were sorted (Fig. 5a and Extended Data Fig. 7a) and analyzed using the PIC-seq algorithm[46]. PIC-seq is an scRNA-seq-based tool that allows transcriptional analysis and deconvolution of cell–cell interactions in comparison to single cells representing the most likely interaction partners, thereby revealing molecular signatures specifically related to physical interaction between cells of interest[46].

Annotation of singlets revealed coherent populations of DCs and T cells with minimal contamination from other cell types, whereas DC–T cell doublet identities represented various combinations of singlet subtypes (Extended Data Fig. 7b,c). First, we analyzed interaction preferences by comparing PIC and singlet transcriptional distributions (Fig. 5b–d). In general PIC and singlet distributions in both healthy and MCDD-fed mice followed patterns previously reported for lymph nodes[46] (Fig. 5c,d). Specifically, we observed preferential pairing of cDC1 and cDC2 subsets and

reduced engagement of proliferating and mature DCs in both conditions (Fig. 5c). Within the T cell compartment, interactions of CD4+ T cells were more enriched in liver lymph nodes of both ND- and MCDD-fed mice and regulatory T cells were preferentially engaged with cDCs in NASH, whereas CD8+ cells were depleted in PICs in both conditions (Fig. 5d). Next, we investigated physical interaction-induced transcriptional signatures by comparing observed gene expression in physical doublets to their expected values based on their PIC-seq assignment to single-cell identities[46] (Fig. 5e). This comparison revealed that DC–T cell interactions in NASH conditions led to a pro-inflammatory expression profile (Fig. 5f–h and Extended Data Fig. 7d,e). For example, cDC-produced *Il12b*, a cytokine critical for development of Th1 responses, was specifically enriched in NASH-derived mDC and mDC^{CCL5hi}–T cell physically interacting pairs compared to the expected *Il12b* production from pairs of mDC and T cells, while in ND condition this enrichment was not observed (Fig. 5f,g). Similarly, MCDD-derived DC–T pairs showed higher production of T cell-derived *Ly6c* and *Nkg7*, linked to CD8+ T cell activation, memory induction and adhesion and DC-derived *Il1b*, a cytokine promoting T cell priming (Fig. 5g,h). mDCs arrive to the lymph nodes loaded with antigens, while lymph-node-resident cDCs capture antigens from organ-derived lymph[38,44]. Liver lymph-node-resident cDC1 cells and, to a lesser extent, cDC2 cells, also showed more inflammatory interaction-induced gene expression in the MCDD condition compared to ND (Extended Data Fig. 7d,e). For example, in cDC1 cells, *Il1b*, as well as chemokines *Ccl5* and *Ccl22* were specifically upregulated in MCDD-derived PICs and not in ND PICs (Extended Data Fig. 7d). Overall, these results suggest that excessive DCs in the NASH liver potentiate pro-inflammatory DC–T cell interactions in liver-draining lymph nodes and promote activation of T cells, especially toward type 1, CD8+ T cell-dependent responses, repetitively linked to worsening of liver pathology in the course of NASH in mouse models[9,10,12] and in humans[30]. In light of these results, we next asked whether manipulating DCs in NASH could shape disease course.

cDC1 blockade attenuates early and advanced NASH pathology. As cDC1 cells were specifically enriched in NASH mouse models, elevated in human blood and liver in NASH and are known to prime CD8+ T cells, previously linked to NASH development and progression[9,10,12], we decided to investigate the impact of cDC1 cells on liver pathology in NASH mouse models. First, we attenuated hepatic cDC1 infiltration by antibody-dependent blockade of XCL1, the major chemokine involved in cDC1 recruitment[47], in a mouse model of NASH induced by CDHFD feeding. At the 5-month time point, CDHFD mice already showed significantly elevated activity of serum ALT and AST, indicating liver injury (Extended Data Fig. 8a). Mice treated with XCL1 antibody for 4 weeks, as compared to an isotype control-treated group, showed a mild decrease in CD11c+MHC-II+CD103+ cells in the liver (Extended Data Fig. 8b). Serum ALT levels in the anti-XCL1-treated group, but not in the control group, were lower compared to the time point before antibody treatment, indicating that partial blockade of cDC1 infiltration to the liver alleviates this hallmark of NASH pathology (Fig. 6a). Serum AST level, a measure of injury in the liver, as well as other organs, followed a similar trend (Extended Data Fig. 8c). Moreover, correlation analysis of hepatic cDC1 counts to various hallmarks of NASH in anti-XCL1-treated and control mice revealed that cDC1 numbers in the liver reflected NAS[40], liver fibrosis (Sirius red staining) and hepatic concentration of triglycerides (Fig.6b and Extended Data Fig. 8d–h). As we previously observed a strong effect of cDCs on T cell activation, we also evaluated numbers of hepatic CD8+ T cells and found them positively correlating with numbers of cDC1 cells (Fig. 6b). Other measures associated with NASH pathology, such as DNA damage marker (γH2AX) and cell stress (p62) were not correlated with numbers of cDCs in the liver (Extended Data Fig. 8h).

To better dissect causality between cDC1 activity and NASH development, we used a mouse model of genetic cDC1 depletion in Xcr1^{DTA} mice, in which activation of the Xcr1 promoter leads to expression of Cre recombinase, which in turn activates expression of cytotoxic diphtheria toxin A, leading to complete ablation of Xcr1-expressing cells. Xcr1$^{Cre\text{-}mTFP1}$ littermates were used as controls[48]. After verifying that Xcr1+ cells are indeed depleted in livers of Xcr1^{DTA} mice (Extended Data Fig. 9a), we sought to determine whether loss of cDC1 cells would affect typical markers of hepatic injury in NASH in a quicker MCDD model. As expected, MCDD feeding for 2 weeks induced liver pathology in control mice, but this effect was abrogated in Xcr1^{DTA} mice lacking cDC1 cells (Fig. 6c and Extended Data Fig. 9b). We found both ALT and AST to be increased in the MCDD condition in control mice, whereas in Xcr1^{DTA} mice AST was not elevated and ALT was increased, but to significantly lower levels than in control MCDD-fed mice (Fig. 6d). As a corollary, loss of cDC1 Xcr1^{DTA} prevented NASH-induced immune rearrangements in the liver, such as an increase in general CD45+ immune cell count in the liver (Extended Data Fig. 9c,d) and the specific increase in CD44+CD62L− effector memory CD8+ T cells, previously linked to NASH progression (Fig.6e and Extended Data Fig. 10a–e)[9,10,49]. These results strongly suggest that cDC1 cells are key in promoting the development of liver pathology in NASH and depletion of cDC1 may mitigate disease. In addition, we observed that cDC1 ablation attenuated other NASH-induced changes in hepatic immune populations, previously suggested to modulate NASH pathology as well, such as CD4+ cells (Extended Data Fig. 10f–j), natural killer (NK) T cells[10], monocytes[10] and platelets[40] (Extended Data Fig. 10k–m). Altogether, these data suggest a key role of cDC1 cells in driving liver pathology, at least in part via their classical role as activators of T cells in NASH.

Fig. 5 | DCs in NASH induce more pro-inflammatory DC–T cell interaction signatures in liver lymph nodes. a, Representative FACS plots of CD45+Lin−MHC-II+CD11c+ cDCs (blue) and TCR-β+ T cell (pink) singlets and CD45+Lin−MHC-II+CD11c+TCR-β+ PICs (purple) purified from liver lymph nodes. **b**, Schematics of the experimental paradigm using PIC-seq to characterize interaction distribution between DCs and T cells. Each PIC is assigned with DC and T cell identities, derived from the singlet populations, of which it is most likely to be composed. The PIC cell type distributions are then compared to the distribution expected based on the singlet populations. **c**,**d**, Distribution of cDC (**c**) and T cell (**d**) subsets in MHC-II+CD11c+ cDC singlets, TCR-β+ singlet T cells and MHC-II+CD11c+TCR-β+ PICs in liver lymph nodes of mice kept on an ND or MCDD for 2 weeks. Cells are pooled from five animals per group. False discovery rate (FDR)-adjusted two-tailed Fisher's exact test. $^{*}P<0.05$; $^{**}P<0.001$; $^{***}P<10\times10^{-5}$. T_{reg}, regulatory T cell. **e**, Schematics of the experimental paradigm using PIC-seq to characterize interaction-specific transcriptional signatures. Observed gene expression of groups of PICs is pooled and compared to the expected value, calculated by summing the expression of the T cell and DC assignments of the PICs. **f**, Gene expression levels in observed PICs assigned to mDC–T cell identity, plotted against expected levels as determined by PIC-seq in liver lymph nodes of mice kept on an ND or MCDD for 2 weeks. Highlighted genes are expressed differentially between observed and expected PICs in one or both conditions. **g**,**h**, Values indicate mean observed (pink) and expected (gray) *Il12β* and *Ly6c2* expression levels in PICs grouped according to their DC subset identities (**g**) and *Nkg7*, *Il1b* and *Il12b* according to their T cell subset identities (**h**) in ND and MCDD conditions. Light and dark gray represent T cell and DC contributions to expected expression, respectively. Error bars indicate 95% confidence intervals by binomial estimation.

Discussion

In this study, we explored the immunological niche of healthy and NASH mouse livers and found that subpopulations of cDCs expand in the early pathology in a murine model of NASH, due to higher proliferation rates of cDC progenitors, CDPs and pre-DCs in bone marrow. Further investigation of distinct mouse models and human liver samples representing a spectrum of NASH, revealed that cDC1 elevation correlated with liver pathology. Using specific deletion of XCR1$^+$ cDC1 cells in a genetic mouse model and partial depletion of cDC1 from the liver using an XCL1-blocking antibody in two different paradigms of NASH induction, we observed that cDC1 cells promote liver inflammation and injury in NASH. Analysis of DC–T cell interacting partners in liver-draining lymph nodes revealed that excessive cDCs may potentiate pro-inflammatory CD8$^+$ T cells, previously linked to NASH exacerbation. Altogether our data suggest that cDC1 cells are important players in NASH (Fig. 6f).

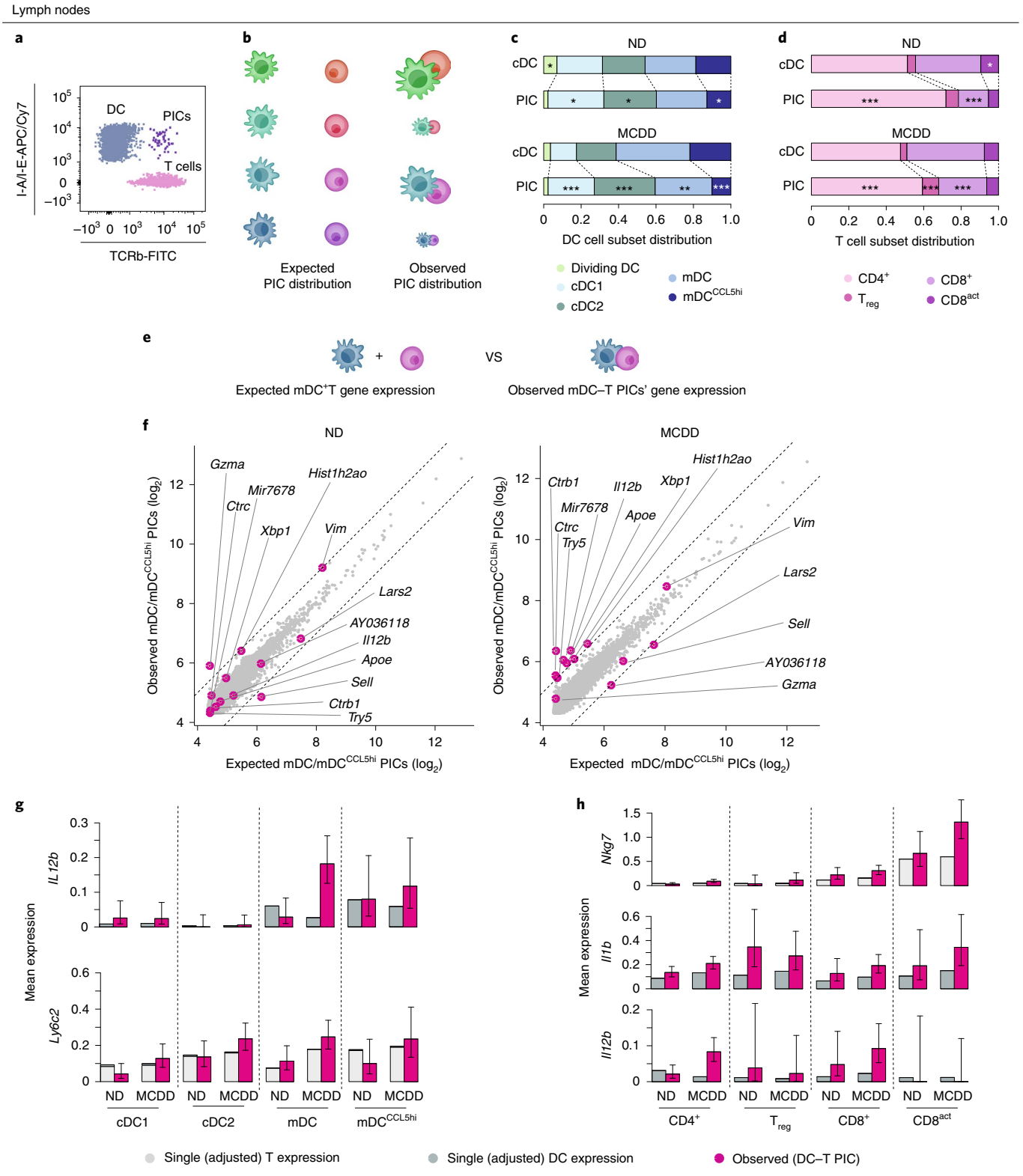

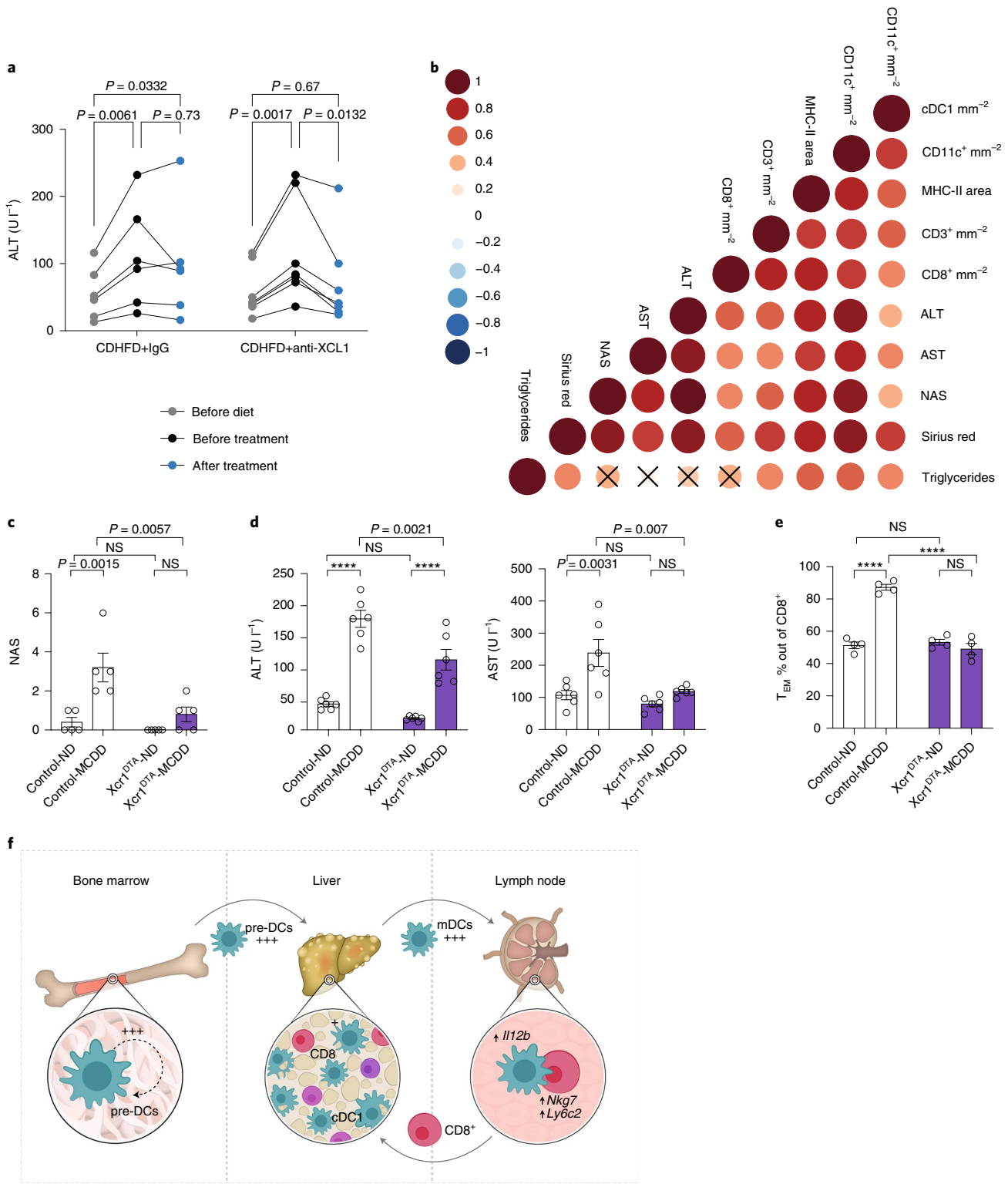

Fig. 6 | Depletion of Xcr1⁺ cDC1 protects the liver from NASH development and progression in diet-induced mouse models of NASH. a, Levels of ALT, a measure of hepatic injury in the serum of wild-type mice before feeding with CDHFD (gray), after 5 months of CDHFD but before treatment (black) and following 4 weeks of anti-XCL1 or control IgG treatment (blue) ($n=6$ mice per group; P values were determined by two-way ANOVA with Tukey's multiple comparisons test). **b**, Correlation analysis between CD103⁺ cDC1 count and NASH pathology parameters in anti-XCL1-treated and IgG-treated mice ($n=12$); two-tailed Spearman correlation (crossed-out points $P>0.05$; color and circle size indicate R^2). **c**, pathological evaluation of NAFLD activity score of in control mice and Xcr1^{DTA} mice (lacking Xcr1⁺ cDC1) fed with an ND or MCDD for 2 weeks ($n=5$ mice per group). **d**, Levels of liver enzymes ALT and AST in serum of control mice and Xcr1^{DTA} mice (lacking Xcr1⁺ cDC1) fed with an ND or MCDD for 2 weeks ($n=6$ mice per group). **e**, FACS-based quantification of CD44⁺CD62L⁻ T cell activated/effector memory (T_{EM}) CD8⁺ T cells in the livers of control and Xcr1^{DTA} mice kept on an ND or MCDD for 2 weeks ($n=4$ mice per group). Data are presented as mean ± s.e.m. (**d**,**e**); NS, nonsignificant; $^{****}P<0.0001$ by one-way ANOVA with Tukey's multiple comparisons test. **f**, Model of systemic cDC activity in NASH.

Earlier studies suggested that CD11c$^+$ cells, including cDCs, prevent development of NASH-related liver inflammation and fibrosis[29,50]. In these studies, depletion of CD11c$^+$ cells in an MCD diet led to worsening of NASH[29], whereas deletion of CD40 on CD11c$^+$ cells in mice fed a WD slightly decreased inflammation but also decreased the numbers of protective Foxp3$^+$ cells and had no effect on steatosis[51]. These effects, however, cannot be directly ascribed to cDCs, as CD11c is also expressed on monocytes and monocyte-derived or resident macrophages, including TREM2$^+$ macrophages, previously suggested to have a protective role in obesity and NAFLD[15,17,31]. Another recent study found that NASH pathology was enhanced in *Batf3*-deficient mice, which lack cDC1 cells[52]. However, *Batf3*-deficent mice can still develop cDC1 cells under inflammatory conditions[53,54] and Batf3 has been implicated in other immune processes potentially involved in NASH pathology, such as establishment of regulatory T cells in the periphery and regulating type 9 helper T cell immunity[55–57], therefore the effects of *Baft3* deletion on NASH pathology cannot be unambiguously ascribed to depletion of cDC1 cells. Our study, using two different NASH mouse models and two approaches to cDC1 blockade based on a highly selective marker expressed only upon pre-cDC1 entry from the blood into peripheral tissues, XCR1 (ref. [48]), indicates pathological function of cDC1 in NASH. Further, another study proposed an antifibrotic role of cDC-derived metalloproteases during the recovery period following carbon tetrachloride-induced liver injury, where expansion of cDCs using Flt3 treatment or adoptive transfer of cDCs promoted liver regeneration[50], pointing to possible contrasting roles of cDCs in NASH establishment and resolution. Altogether, these examples highlight the importance of careful selection of markers and genetic tools for functional studies, especially in cells undergoing dynamic phenotypic changes throughout their short lifespan, such as cDCs and in chronic diseases, where the nature of pathology and cellular contributions to it may change over time.

In parallel to our findings in mouse models, our study also revealed NASH-related changes in the cDC compartment in human blood and liver. Previous reports examining human NASH livers using microarrays reported that enhanced cDC signatures correlated with liver pathology, but failed to detect markers of a rare cDC1 subset[30]. Others reported changing cDC proportions at the possible end points of NASH: analyses of human primary and early relapse hepatocellular carcinoma (HCC) identified DCs as important modulators of the tumor microenvironment and potential drivers of local T cell and NK cell dysfunction[58,59], whereas no enrichment for cDCs was found in cirrhosis[19]. These results, in accordance with above-mentioned studies in mouse models, suggest that the number and role of cDCs may change depending on the trajectory along which the liver pathology progresses.

Finally, we investigated cDC–T cell interactions as the mechanistic link between the excess of cDCs and liver pathology in NASH. However, recent research suggested that cDCs shape immunity beyond instructing T cells. cDCs were proposed to activate NK cells and to possibly recruit neutrophils[38], cell types that may play a role in NASH establishment[60,61]. cDC2 cells can stimulate sensory neurons in the skin to promote itch, while in the lymph node, cDCs promote formation of high endothelial venules and directly influence the properties of stromal cells, thereby supporting structural changes in lymph node architecture accompanying an immune response[38]. The role of such interactions in NASH, where stromal remodeling and fibrosis are key hallmarks of the disease, will be an interesting avenue for future research.

In our study, however, we focused on the classical role of cDCs as instructors of T cells. In NASH conditions, DC–T cell interactions in liver-draining lymph nodes specifically promoted activation of T cells, immune cells shown to accumulate in the liver in humans with NASH and in NASH animal models[9–11,13] and to promote NASH via direct interaction with hepatocytes[10,13] and profibrotic activation of hepatic stellate cells[11]. Accordingly, numbers of cDC1 cells in the liver correlated with numbers and activation of hepatic CD8$^+$ cells; however, this did not correlate with molecular markers of hepatic injury, such as DNA damage marker (γH2AX) and cell stress (p62), suggesting additional mechanisms that may play a role in cDC- and T cell-induced NASH pathology. Recent work discovered the presence of auto-aggressive CD8$^+$CXCR6$^+$ T cells, which promote NASH pathology in an MHC-I-independent manner[13]. Finally, CD8$^+$ T cell activity in NASH promoted HCC development and progression[12], whereas formation of ectopic lymphoid structures within the liver was associated with poor survival in patients with HCC and in mouse models[62]. These results suggest that liver immunology may be governed by potentially several non-canonical immune mechanisms; the role of cDCs in the context of advanced NASH and its progression to HCC will be the subject of future research.

With these caveats, nevertheless, our data indicate that excessive cDC1 cells observed in livers of patients with NASH and in animal models promote liver pathology, at least in part via their interaction with T cells. In light of these results, we suggest cDC1 modulation as a possible future immunotherapy approach to NASH.

Online content

Any methods, additional references, Nature Research reporting summaries, source data, extended data, supplementary information, acknowledgements, peer review information; details of author contributions and competing interests; and statements of data and code availability are available at https://doi.org/10.1038/s41591-021-01344-3.

Received: 16 June 2020; Accepted: 9 April 2021;
Published online: 20 May 2021

References

1. Brunt, E. M. et al. Nonalcoholic fatty liver disease. *Nat. Rev. Dis. Prim.* **1**, 15080 (2015).
2. Diehl, A. M. & Day, C. Cause, pathogenesis, and treatment of nonalcoholic steatohepatitis. *N. Engl. J. Med.* **377**, 2063–2072 (2017).
3. Anstee, Q. M., Reeves, H. L., Kotsiliti, E., Govaere, O. & Heikenwälder, M. From NASH to HCC: current concepts and future challenges. *Nat. Rev. Gastroenterol. Hepatol.* **16**, 411–428 (2019).
4. Friedman, S. L., Neuschwander-Tetri, B. A., Rinella, M. & Sanyal, A. J. Mechanisms of NAFLD development and therapeutic strategies. *Nat. Med.* **24**, 908–922 (2018).
5. Chalasani, N. et al. The diagnosis and management of nonalcoholic fatty liver disease: practice guidance from the American Association for the Study of Liver Diseases. *Hepatology* **67**, 328–357 (2018).
6. Macpherson, A. J., Heikenwälder, M. & Ganal-Vonarburg, S. C. The liver at the nexus of host-microbial interactions. *Cell Host Microbe* **20**, 561–571 (2016).
7. Krenkel, O. & Tacke, F. Liver macrophages in tissue homeostasis and disease. *Nat. Rev. Immunol.* **17**, 306–321 (2017).
8. Nishimura, S. et al. CD8$^+$ effector T cells contribute to macrophage recruitment and adipose tissue inflammation in obesity. *Nat. Med.* **15**, 914–920 (2009).
9. Bhattacharjee, J. et al. Hepatic natural killer T-cell and CD8$^+$ T-cell signatures in mice with nonalcoholic steatohepatitis. *Hepatol. Commun.* **1**, 299–310 (2017).
10. Wolf, M. J. et al. Metabolic activation of intrahepatic CD8$^+$ T cells and NKT cells causes nonalcoholic steatohepatitis and liver cancer via cross-talk with hepatocytes. *Cancer Cell* **26**, 549–564 (2014).
11. Breuer, D. A. et al. CD8$^+$ T cells regulate liver injury in obesity-related nonalcoholic fatty liver disease. *Am. J. Physiol. Gastrointest. liver Physiol.* **318**, g211–g224 (2020).
12. Pfister, D. et al. NASH limits anti-tumor surveillance in immunotherapy-treated HCC. *Nature* https://doi.org/10.1038/s41586-021-03362-0 (2021).
13. Dudek, M. et al. Auto-aggressive CXCR6$^+$ CD8 T cells cause liver immune pathology in NASH. *Nature* https://doi.org/10.1038/s41586-021-03233-8 (2021).
14. Hart, K. M. et al. Type 2 immunity is protective in metabolic disease but exacerbates NAFLD collaboratively with TGF-β. *Sci. Transl. Med.* **9**, eaal3694 (2017).

15. Jaitin, D. A. et al. Lipid-associated macrophages control metabolic homeostasis in a TREM2-dependent manner. *Cell* **178**, 686–698 (2019).
16. Parhizkar, S. et al. Loss of TREM2 function increases amyloid seeding but reduces plaque-associated ApoE. *Nat. Neurosci.* **22**, 191–204 (2019).
17. Xiong, X. et al. Landscape of intercellular crosstalk in healthy and NASH liver revealed by single-cell secretome gene analysis. *Mol. Cell* **75**, 644–660 (2019).
18. Perugorria, M. J. et al. Non-parenchymal TREM-2 protects the liver from immune-mediated hepatocellular damage. *Gut* **68**, 533 (2019).
19. Ramachandran, P. et al. Resolving the fibrotic niche of human liver cirrhosis at single-cell level. *Nature* https://doi.org/10.1038/s41586-019-1631-3 (2019).
20. Montandon, S. A. et al. Multi-technique comparison of atherogenic and MCD NASH models highlights changes in sphingolipid metabolism. *Sci. Rep.* **9**, 16810 (2019).
21. Reid, D. T. & Eksteen, B. Murine models provide insight to the development of non-alcoholic fatty liver disease. *Nutr. Res. Rev.* **28**, 133–142 (2015).
22. Baran, Y. et al. MetaCell: analysis of single-cell RNA-seq data using k-NN graph partitions. *Genome Biol.* **20**, 206 (2019).
23. Reid, D. T. et al. Kupffer cells undergo fundamental changes during the development of experimental NASH and are critical in initiating liver damage and inflammation. *PLoS ONE* **11**, e0159524 (2016).
24. Tran, S. et al. Impaired Kupffer cell self-renewal alters the liver response to lipid overload during non-alcoholic steatohepatitis. *Immunity* **53**, 627–640 (2020).
25. Devisscher, L. et al. Non-alcoholic steatohepatitis induces transient changes within the liver macrophage pool. *Cell. Immunol.* **322**, 74–83 (2017).
26. Zang, S. et al. Neutrophils play a crucial role in the early stage of nonalcoholic steatohepatitis via neutrophil elastase in mice. *Cell Biochem. Biophys.* **73**, 479–487 (2015).
27. Krenkel, O. et al. Myeloid cells in liver and bone marrow acquire a functionally distinct inflammatory phenotype during obesity-related steatohepatitis. *Gut* **69**, 551–563 (2020).
28. Liaskou, E. et al. Monocyte subsets in human liver disease show distinct phenotypic and functional characteristics. *Hepatology* **57**, 385–398 (2013).
29. Henning, J. R. et al. Dendritic cells limit fibroinflammatory injury in nonalcoholic steatohepatitis in mice. *Hepatology* **58**, 589–602 (2013).
30. Haas, J. T. et al. Transcriptional network analysis implicates altered hepatic immune function in NASH development and resolution. *Nat. Metab.* **1**, 604–614 (2019).
31. Remmerie, A. et al. Osteopontin expression identifies a subset of recruited macrophages distinct from Kupffer cells in the fatty liver. *Immunity* **53**, 641–657 (2020).
32. Daemen, S. et al. Dynamic shifts in the composition of resident and recruited macrophages influence tissue remodeling in NASH. *Cell Rep.* **34**, 108626 (2021).
33. Guilliams, M. et al. Unsupervised high-dimensional analysis aligns dendritic cells across tissues and species. *Immunity* **45**, 669–684 (2016).
34. Mederacke, I., Dapito, D. H., Affò, S., Uchinami, H. & Schwabe, R. F. High-yield and high-purity isolation of hepatic stellate cells from normal and fibrotic mouse livers. *Nat. Protoc.* **10**, 305–315 (2015).
35. Trak-Smayra, V. et al. Pathology of the liver in obese and diabetic ob/ob and db/db mice fed a standard or high-calorie diet. *Int J. Exp. Pathol.* **92**, 413–421 (2011).
36. Febbraio, M. A. et al. Preclinical models for studying NASH-driven HCC: how useful are they? *Cell Metab.* **29**, 18–26 (2019).
37. Farrell, G. et al. Mouse models of nonalcoholic steatohepatitis: toward optimization of their relevance to human nonalcoholic steatohepatitis. *Hepatology* **69**, 2241–2257 (2019).
38. Cabeza-Cabrerizo, M., Cardoso, A., Minutti, C. M., Pereira da Costa, M. & Reis e Sousa, C. Dendritic cells revisited. *Ann. Rev. Immunol.* https://doi.org/10.1146/annurev-immunol-061020-053707 (2021).
39. Lavin, Y. et al. Tissue-resident macrophage enhancer landscapes are shaped by the local microenvironment. *Cell* **159**, 1312–1326 (2014).
40. Malehmir, M. et al. Platelet GPIbα is a mediator and potential interventional target for NASH and subsequent liver cancer. *Nat. Med.* **25**, 641–655 (2019).
41. Schlitzer, A., McGovern, N. & Ginhoux, F. in *Seminars* in *Cell & Developmental Biology* Vol. 41 9–22 (Elsevier, 2015).
42. Schultze, J. L., Mass, E. & Schlitzer, A. Emerging principles in myelopoiesis at homeostasis and during infection and inflammation. *Immunity* **50**, 288–301 (2019).
43. Schlitzer, A. et al. Identification of cDC1- and cDC2-committed DC progenitors reveals early lineage priming at the common DC progenitor stage in the bone marrow. *Nat. Immunol.* **16**, 718–728 (2015).
44. Nutt, S. L. & Chopin, M. Transcriptional networks driving dendritic cell differentiation and function. *Immunity* **52**, 942–956 (2020).
45. Yu, J. et al. The differential organogenesis and functionality of two liver-draining lymph nodes in mice. *J. Autoimmun.* **84**, 109–121 (2017).
46. Giladi, A. et al. Dissecting cellular crosstalk by sequencing physically interacting cells. *Nat. Biotechnol.* **38**, 629–637 (2020).
47. Böttcher, J. P. et al. NK cells stimulate recruitment of cDC1 into the tumor microenvironment promoting cancer immune control. *Cell* **172**, 1022–1037 (2018).
48. Wohn, C. et al. Absence of MHC class II on cDC1 dendritic cells triggers fatal autoimmunity to a cross-presented self-antigen. *Sci. Immunol.* **5**, eaba1896 (2020).
49. Ghazarian, M. et al. Type I interferon responses drive intrahepatic T cells to promote metabolic syndrome. *Sci. Immunol.* **2**, eaai7616 (2017).
50. Jiao, J. et al. Dendritic cell regulation of carbon tetrachloride-induced murine liver fibrosis regression. *Hepatology* **55**, 244–255 (2012).
51. Aarts, S. et al. Depletion of CD40 on CD11c$^+$cells worsens the metabolic syndrome and ameliorates hepatic inflammation during NASH. *Sci. Rep.* **9**, 14702 (2019).
52. Heier, E.-C. et al. Murine CD103$^+$dendritic cells protect against steatosis progression towards steatohepatitis. *J. Hepatol.* **66**, 1241–1250 (2017).
53. Tussiwand, R. et al. Compensatory dendritic cell development mediated by BATF–IRF interactions. *Nature* **490**, 502–507 (2012).
54. Seillet, C. et al. CD8α$^+$DCs can be induced in the absence of transcription factors Id2, Nfil3, and Batf3. *Blood* **121**, 1574–1583 (2013).
55. Lee, W., Kim, H. S., Hwang, S. S. & Lee, G. R. The transcription factor Batf3 inhibits the differentiation of regulatory T cells in the periphery. *Exp. Mol. Med.* **49**, e393–e393 (2017).
56. Li, J. et al. IL-9 and Th9 cells in health and diseases—from tolerance to immunopathology. *Cytokine Growth Factor Rev.* **37**, 47–55 (2017).
57. Świderska, M. et al. The interplay between Th17 and T-regulatory responses as well as adipokines in the progression of non-alcoholic fatty liver disease. *Clin. Exp. Hepatol.* **3**, 127–134 (2017).
58. Zhang, Q. et al. Landscape and dynamics of single immune cells in hepatocellular carcinoma. *Cell* **179**, 829–845 (2019).
59. Sun, Y. et al. Single-cell landscape of the ecosystem in early-relapse hepatocellular carcinoma. *Cell* **184**, 404–421 (2021).
60. Zang, S. et al. Neutrophils play a crucial role in the early stage of nonalcoholic steatohepatitis via neutrophil elastase in mice. *Cell Biochem. Biophys.* **73**, 479–487 (2015).
61. Tosello-Trampont, A. C. et al. NKp46(+) natural killer cells attenuate metabolism-induced hepatic fibrosis by regulating macrophage activation in mice. *Hepatology* **63**, 799–812 (2016).
62. Finkin, S. et al. Ectopic lymphoid structures function as microniches for tumor progenitor cells in hepatocellular carcinoma. *Nat. Immunol.* **16**, 1235–1244 (2015).

Methods

Mice. Wild-type (WT) C57Bl/6 mice were purchased from Harlan and housed in the Weizmann Institute animal facility or purchased from Charles River and housed at the German Cancer Research Center (DKFZ). Animals were maintained under specific-pathogen-free conditions. Xcr1^{DTA} mice were created by crossing homozygote Xcr1$^{Cre\text{-}mTFP148}$ to DTA$^{+/+}$ (B6.129P2-Gt(ROSA)26Sor$^{tm1(DTA)Lky}$/J). Xcr1$^{Cre\text{-}mTFP1}$ and DTA$^{+/+}$ mice were a kind gift from B. Malissen. *Ob/Ob* mice and *Db/Db* mice were a kind gift from E. Elinav. All mice were provided with chow and water ad libitum and housed under a strict 12-h light–dark cycle. For liver pathology induction 8–9-week-old mice were fed with normal chow or with an MCDD (TD.90262, Envigo Teklad Diets) for 2, 4 or 8 weeks, HFD (D12451; Research Diets) for 6 months, CDHFD (D05010402: Research Diets) for 6 months or WD with trans-fat (D16022301i; Research Diets) for 3 or 6 months. All experimental procedures were performed in accordance to Institutional Animal Care and Use Committee of the Weizmann Institute of Science and German Law (G141/19 and G129/16).

Isolation of leukocytes from mouse tissues. Mice were fasted for 14 h and anesthetized with an intraperitoneal (i.p.) injection of a ketamine (100 mg kg^{-1}) and xylazine (10 mg kg^{-1}) mixture. Liver leukocytes were isolated by a modification of the two-step collagenase perfusion method of Seglen Digestion using Liberase TL (cat. no. 5401020001; Roche)[63] for scRNA-seq or using The Liver Dissociation kit (cat. no. 130-105-807; Miltenyi Biotec) according to the manufacturer's guidelines for FACS analyses. Bone marrow was isolated by flushing from tibia and femur. Celiac and portal lymph nodes[45] were processed for recovery of DC–T cell PICs and single DCs and T cells as previously described[46]. Briefly, lymph nodes were digested in Isocove's modified Dulbecco's medium (Sigma-Aldrich) supplemented with Liberase TL (100 µg ml^{-1}, Roche) and DNase I (100 µg ml^{-1}, Roche) at 37 °C for 20 min and dissociated with 18G and 21G needles. Blood was sampled from the inferior vena cava or by retro-orbital bleeding. Red blood cell lysis was performed on bone marrow and blood samples (RBC Lysis Buffer, Invitrogen). Isolated leukocytes stained cell surface markers for flow cytometry analysis and sorting.

Human blood samples. Blood samples were drawn from patients with chronic liver disease recruited at Chaim Sheba Tel-Hashomer Liver Diseases Center. The study was approved by the Institutional Review Board of the Chaim Sheba Medical Center and was carried out according to local guidelines and regulations. Before patient inclusion, written informed consent was obtained. The diagnosis of NAFLD was based on ultrasound evaluation. NASH diagnosis was based on the presence of ballooning, steatohepatitis and fibrosis on liver biopsy, when it was available or on the presence of fibrosis by noninvasive liver assessment. Peripheral blood for FACS analysis (3–5 ml) was collected in EDTA-containing tubes (Becton Dickinson). Each sample was diluted 1:1 in ice-cold FACS buffer. Mononuclear cell separation was performed by density centrifugation medium (Ficoll-Paque; GE Healthcare Life Sciences) in a 1:1 ratio with diluted blood cells. Centrifugation (460*g*, 25 min) was performed at 10 °C and mononuclear cells were carefully aspirated and washed with ice-cold FACS buffer. After red blood cell lysis (Sigma-Aldrich) for 5 min at 4 °C and washing, cells were frozen in 10% dimethylsulfoxide in FBS and stored at −80 °C until further processing. On the day of analysis, cells were washed twice with FACS buffer, stained and analyzed using BD FACSDiva software v.9.0 (BD Bioscience) and FlowJo software v.10.7.1 (FlowJo, LLC).

Human liver samples. Following Institutional Review Board approval by the Medical Ethics Committee of Heidelberg University (ref. no. S-629/2013), human liver tissue samples (and matching blood samples for ALT and ASP analysis) were collected from patients undergoing bariatric surgery at the Department of Surgery at Heidelberg University Hospital. Liver sections were stained for H&E in the division of Chronic Inflammation and Cancer, DKFZ and NAS score was evaluated by an experienced liver pathologist (A. Weber, University of Zürich).

FACS analysis and single-cell capture. For mouse single-cell or PIC sorting, cells after dissociation were washed and suspended in cold FACS buffer (0.5% BSA and 2 mM EDTA in PBS), stained with fluorophore-conjugated antibodies and filtered through a 100-µm strainer. Before sorting, cells were stained with DAPI to exclude dead/dying cells. Cells were sorted with a SORP-FACSAria II flow cytometer (BD Biosciences) using a 100-µm nozzle, gating for specific populations (as indicated for each experiment) after exclusion of dead cells (based on DAPI) and doublets (based on pulse width; except for PIC sorting, where the doubles exclusion step was omitted). Single cells or PICs were sorted into 384-well capture plates containing 2 µl of lysis solution and barcoded poly(T) reverse transcription primers for scRNA-seq as described previously. Immediately after sorting, plates were spun down to ensure cell immersion into the lysis solution, snap-frozen on dry ice and stored at −80 °C until further processing[64].

Liver biopsies from patients undergoing bariatric surgery were collected in RPMI (supplemented with 10% FBS) and immediately transported on ice to the laboratory. A section of tissue was formalin fixed for histopathological evaluation, but the bulk of the tissue was digested using a Miltenyi tumor dissociation kit (cat. no. 130-095-929) as per manufacturer's instructions. Single-cell suspensions thus generated were stored in liquid nitrogen in FBS + 20% dimethylsulfoxide until further processing. For sorting and scRNA-seq of DCs obtained from control and NASH livers, stored cells were thawed in a 37 °C water bath, washed once with complete medium and once with FACS buffer (PBS + 2% FBS). After Fc blocking, cells were stained for 30 min and washed once with FACS buffer and once with sorting buffer (PBS + 0.5 mM EDTA). Sorting was carried out at the DKFZ cytometry facility using a BD FACSAria. Bulk-sorted CD45^{+}Lin^{-}CD11c^{+} cells were then processed for 10X (10X Genomics).

For marker-based validations and sorting of specific DC populations, mouse samples were stained using the following antibodies: BV711 or PE-Dazzle-conjugated CD45 (clone 30-F11) marking leukocytes, eFluor450-conjugated CD3 (clone 17A2), CD19 (clone 1D3), B220 (clone RA3-6B2), NK1.1 (clone PK136), Ly6g (clone 1A8), Ly6c (clone HK1.4) and Ter119 (clone Ter119) to exclude T cells, B cells, NK cells, neutrophils, monocytes and erythrocytes, PE or PE-Dazzle-conjugated CD11c (clone N418), FITC- or APC-Cy7-conjugated I-A/I-E (clone M5/114.15.2), Brilliant Violet 650-conjugated CD11b (clone M1/70), PE-conjugated CD103 (clone 2E7), APC-conjugated XCR1 (clone ZET), APC-conjugated CCR7 (clone 4B12), PE/Cy7-conjugated CD83 (clone Michel-19) and PE/Cy7-conjugated CD86 (clone GL-1). DAPI, detected in the same channel with lineage staining, was used for live/dead cell detection.

For marker-based validations and sorting of pre-DC populations Ly6c was omitted in the lineage mix. Additionally, the following antibodies were used: PE-conjugated CD135 (FLT3; clone A2F10), PE-Cy7- or PE-conjugated CD115 (clone AFS98), APC/Cy7-conjugated Ly6c (clone HK1.4) and APC/Cy7-conjugated c-kit (clone 2B8). For T cell analysis and PIC sorting, the following antibodies were used: PE-Dazzle or FITC-conjugated CD45 (clone 30-F11), PE-Dazzle or PE-conjugated CD11c (clone N418), FITC- or APC-Cy7-conjugated I-A/I-E (clone M5/114.15.2), FITC-or PE- conjugated TCR-β (clone H57-597), eFluor450-conjugated CD4 (clone GK1.5), PE-Cy7-conjugated CD8 (clone 53-6.7), PE-Cy5-conjugated CD62L (clone DREG-56) and APC-conjugated CD44 (clone IM7). For NKT cell analysis, FITC-conjugated CD45 (clone 30-F11), eFluor450-conjugated CD3 (clone 17A2) and PE-conjugated NK1.1 (clone PK.126) were used. For monocyte analysis FITC-conjugated CD45 (clone 30-F11), PerCP-Cy5.5-conjugated Ly6C (clone HK1.4) and Brilliant Violet 650-conjugated CD11b (clone M1/70) were used. For these analyses, DAPI, detected in the same channel with lineage staining, was used for live/dead cell detection.

For human blood DC analysis, the following antibodies were used: PerCP-Cy5.5-conjugated CD45 (clone H130), FITC-conjugated CD1c (clone L161), APC-conjugated CD11c (clone B-ly6), APC/Cy7-conjugated CD14 (clone MOPg), BV570-conjugated HLA-DR (clone L243), PE-Dazzle-conjugated CD141 (clone M80) and PE/Cy7-conjugated CD19 (clone J3-119). DAPI, detected in the same channel with lineage staining, was used for live/dead cell detection.

For human DC sorting from the liver, the following antibodies were used: PE-conjugated CD45 (clone H130), FITC-conjugated Anti-Human Lineage Cocktail 3 (lin 3; including anti-CD3, anti-CD14, anti-CD19 and anti-CD20; BD Biosciences cat. 643510) and BV421-conjugated CD11c (clone 3.9) along with the live/dead stain (Thermo Fisher Scientific, L34973).

All antibodies were purchased from eBioscience or BioLegend. Cells were analyzed using BD FACSDIVA software (BD Bioscience) and FlowJo software (FlowJo, LLC).

Cell cycle analysis. Cell cycle analysis based on BrdU incorporation was performed as previously described[65]. Mice were injected i.p. with 1 mg of BrdU (BD Pharmingen), per manufacturer's instructions, 10 h before cell extraction. Immune cells from the liver, bone marrow and blood were isolated as indicated above. BrdU analysis was performed using a BrdU Flo Kit (BD Pharmingen) according to manufacturer's instructions and with the following modifications: DNase I digestion was performed for 90 min and intracellular staining was performed for 60 min[65]. Cells were analyzed using an LSRII and FlowJo software (FlowJo, LLC).

Anti-XCL1 treatment. For neutralization of XCL1, 50 µg of anti-XCL1 (R&D systems MAB486) or isotype-matched control antibodies (R&D systems MAB006) were injected i.p. twice a week for 4 weeks (total of eight injections).

Immunofluorescence. Mice were perfused with cooled PBS and single liver lobes were dissected and fixed in cooled 4% PFA solution for 4 h, washed three times and then transferred to 30% sucrose solution for 48 h. Tissues were then embedded in optimal cutting temperature compound (Tissue-Tek) and 10-µm thick sections were sliced using a LEICA CM1950 machine and mounted on SuperFrost Plus slides (Thermo Fisher Scientific). For visualization of DCs, sections were first washed in PBS three times and blocked with a blocking buffer solution (5% FBS, 1% BSA and 0.2% Triton) for 2 h at room temperature and incubated with PE or APC-conjugated anti-CD11c (clone N418), FITC-conjugated anti-I-A/I-E (clone M5/114.15.2), APC-conjugated Xcr1 (clone ZET) and APC-conjugated CD31 (clone MEC13.3), PE-conjugated CD103 (clone 2E7), all diluted 1:100 in blocking buffer (BioLegend) at 4 °C overnight. Next, sections were washed three times with PBST and DAPI reagent was added for 10 min to detect cell nuclei. Sections were washed once in PBST, mounted with SlowFade (Invitrogen) and sealed with coverslips. Microscopic analysis was performed using a laser-scanning confocal

microscope (Zeiss, LSM880). Images were acquired and processed with the same threshold settings across samples using Imaris 9.7 (Bitplane).

Histology, immunohistochemistry, scanning and automated analysis. The procedure was performed as described elsewhere[40]. Briefly, 2-µm sections from FFPE were stained with H&E, IHC or immunofluorescence antibodies (mouse: CD42b, 1:200 dilution, SP219, cat. ab183345; CD4, 1:1,000 dilution, 4SM95, cat. 14-9766; CD8, 1:200 dilution, 4SM15, cat. 14-0808-82; CD11c, 1:5,000 dilution, D1V9Y, BD cat. 553799; MHC-II, 1:500 dilution, M5/114.15.2, Novus Biological cat. NBP1-43312; CD3, 1:500 dilution, SP7, Invitrogen cat. MA1-90582; γH2AX, 1:500 dilution, Novus Biol, cat. NB100-2280; p62, 1:500 dilution, Biozol Diagnostica cat. MBL-PM045; human: CD141, 1:100 dilution, E7Y9P, Cell Signaling cat. 43514 and CD31, 1:40 dilution, JC70A, Dako cat. M0823). For fibrosis evaluation, slides were stained in an automated multistainer (Leica ST5020) according to the following program: (1) Deparaffinization using xylol 100% > ethanol 100% > ethanol 96% > ethanol 70%. (2) Hematoxylin counterstain for 10 min. (3) Wash in tap water for 8 min. (4) Incubation in Sirius A reagent for 1 h. (5) Wash in acetic acid for 1 min for two cycles. (6) Dehydration in ethanol 100% > xylol 100%. Slides were scanned using an Aperio System and analyzed using Aperio Image Scope software 12.4.0. NAS was evaluated as previously described for murine livers[12,40] and human liver sections[66].

Concentration of ALT and AST in mouse blood serum. Blood was obtained from the inferior vena cava by retro-orbital bleeding. Serum was isolated by centrifugation (10,000*g* at 4 °C for 20 min). Biochemical markers of liver functions AST and ALT in the serum were determined using a Cobas c111 analyzer by Roche or by a Fuji DRI-CHEM NX500i machine with commercially available test application from FUJIFILM for ALT and AST measurement.

Intra-hepatic triglyceride measurement. Intra-hepatic triglyceride concentration measurement was performed with a commercially available kit (Sigma-Aldrich, cat. no. MAK266) on snap-frozen liver tissue according to the manufacturer instructions.

Single-cell library preparation. scRNA-seq libraries from mouse cells were prepared with modified massively parallel scRNA-seq method (MARS-seq)[64]. In brief, messenger RNA from single cells sorted into cell capture plates was barcoded, converted into cDNA and pooled using an automated pipeline. Subsequently, the pooled sample was amplified and the resulting material was fragmented and converted into a sequencing-ready library by tagging the samples with pool barcodes and Illumina sequences. Each pool of cells was tested for library quality and library concentration was assessed. scRNA-seq libraries from human liver dendritic cells were prepared with 10X v.3.1 kit (10X Genomics) according to the manufacturer's guidelines.

Single-cell RNA analysis. scRNA-seq libraries (pooled at an equimolar concentration) were sequenced on an Illumina NextSeq 500 or NovaSeq 6000 at a median sequencing depth of 20,000 reads per cell. Sequences were mapped to the mouse (mm10) or human (GRCh38-1.2.0) genome using Cell Ranger v.3.0.0.

For MARS-seq, demultiplexing and filtering was performed as previously described[64], with the following adaptations. Mapping of reads was performed using HISAT (v.0.1.6); reads with multiple mapping positions were excluded. Reads were associated with genes if they were mapped to an exon, using the Ensembl gene annotation database (EMBL release 90). The level of spurious UMIs in the data was estimated by using statistics on empty MARS-seq wells. For both MARS-seq and 10X, cells with <500 UMIs or >20% mitochondrial genes or mitochondrial genes being the most differential were discarded from the analysis. For PIC-seq, cells with <1,000 UMIs were discarded. All downstream analysis was performed in R.

Metacell pipeline. The metacell pipeline[22], was used to derive informative genes and to compute cell-to-cell similarity, to compute k-NN graph covers and derive distribution of RNA in cohesive groups of cells (or metacells) and to derive strongly separated clusters using bootstrap analysis and computation of graph covers on resampled data. We removed specific mitochondrial genes, immunoglobulin genes and genes linked with poorly supported transcriptional models (annotated with the prefix 'Rp-'). Gene features were selected using the threshold value for the normalized var/mean (Tvm) = 0.3 and a minimum total UMI count >50. We subsequently performed hierarchical clustering of the correlation matrix between metacells and grouped them into clusters representing cell types and states. We used $K = 100$, 500 bootstrap iterations and otherwise standard parameters.

Density plot. To generate density plots we used R function kde2d from package MASS that conducts two-dimensional kernel density estimation with an axis-aligned bivariate normal kernel, evaluated on a square grid. For each sample we calculated normalized densities to account for variable cell numbers.

Replication score. The proliferation score for each metacell is defined as the average expression of cell cycle gene signature as previously described[67], normalized by the number of cells in each metacell.

PIC-seq. Assignment of PICs to their T cell and DC identities was performed as previously described with necessary adjustments[46]. In short, PICs are modeled as a linear mixture of pairs of contributing cells. Each contributing cell (T cell or DC) belongs to a metacell from the respective T cell or DC background models calculated over the singlet populations and its gene expression is sampled from the multinomial probability distribution of that metacell. The mixing factor (α) assigned for each PIC, denotes the fraction of UMIs contributed by the T cell to that PIC.

The PIC-seq algorithm operates in two steps. First, it applies a linear regression model trained on synthetic PICs to infer α for each PIC. Second, it constructs all possible combinations of metacells from populations A and B mixed by α and calculates the expected gene expression distributions of these mixtures. A maximum likelihood estimator is applied to each PIC to derive two metacells whose mixture is most likely to give rise to the PIC.

To derive genes that would serve as features for linear regression, we computed gene correlation with each cell's UMI count, for T cells and DCs separately. We selected the top 100 most UMI-correlated genes in T cells and DCs, as well as genes used as features in the metacell cover (removing ribosomal and poorly annotated genes), retaining 364 (Supplementary Table 1) features. Both synthetic and real PIC matrices were downsampled to 1,000 UMIs per cell (numis = 1,000). The R^2 value for estimating the mixing coefficient over the synthetic PIC was 61%

At the second step, PIC-seq chooses for each PIC its best assignment of contributing T cell and DC metacells, implementing a maximum likelihood estimator. To derive genes for computing the maximum likelihood estimator assignment, we chose the top 20 differential genes in each T cell (or DC)-associated metacell, whose mean expression was at least 1.74-fold higher than the median across all T cell (or DC) metacells. We combined this set of genes with the genes used as features in the metacell cover, but discarded genes that are highly differential both in the T cell and DC metacell models (more than 1.74-fold enrichment in at least one metacell in each population), as well as ribosomal and poorly annotated genes, retaining 287 genes (Supplementary Table 1).

We then reconstructed the expected levels of a gene in each PIC as previously described[46]. In short, the expected expression of each gene in a certain PIC equals the α-weighted sum of the contribution from the T cell part (which can be estimated from the characteristic multinomial distribution of the contributing T metacell) and the contribution from the DC part. We used an FDR-adjusted chi-squared test to systematically scan for genes whose observed values diverge from expected in specific groups of PIC ($q < 10^{-5}$).

Statistical analyses. Differential gene expression analysis was performed on UMIs divided by the median UMI count using a Mann–Whitney *U*-test with FDR correction. Cell population abundancies, metabolic and pathology parameters in Figs. 2–6 were compared with a two-tailed Student's *t*-test and one- or two-way ANOVA. The relationship between cDC1 cell abundance and liver pathology parameters in Figs. 3e and 6b and Extended Data Fig. 8h was determined using a two-tailed Spearman correlation. Statistical calculations of cell population abundance and metabolic parameter comparisons were performed using GraphPad Prism 8.

Reporting Summary. Further information on research design is available in the Nature Research Reporting Summary linked to this article.

Data availability

The scRNA-seq data generated in this study are available at the Gene Expression Omnibus under accession GSE169447.

Code availability

The Metacell package is available at https://github.com/tanaylab/metacell. The PIC-seq analysis package is available at https://github.com/aygoldberg/PIC-seq.

References

63. Halpern, K. B. et al. Single-cell spatial reconstruction reveals global division of labour in the mammalian liver. *Nature* **542**, 352–356 (2017).
64. Keren-Shaul, H. et al. MARS-seq2.0: an experimental and analytical pipeline for indexed sorting combined with single-cell RNA sequencing. *Nat. Protoc.* **14**, 1841–1862 (2019).
65. Soucie, E. L. et al. Lineage-specific enhancers activate self-renewal genes in macrophages and embryonic stem cells. *Science* **351**, aad5510 (2016).
66. Kleiner, D. E. et al. Design and validation of a histological scoring system for nonalcoholic fatty liver disease. *Hepatology* **41**, 1313–1321 (2005).
67. Giladi, A. et al. Single-cell characterization of haematopoietic progenitors and their trajectories in homeostasis and perturbed haematopoiesis. *Nat. Cell Biol.* **20**, 836–846 (2018).

Acknowledgements

We thank T. Wiesel and T. Bigdary from the Scientific Illustration unit of the Weizmann Institute for artwork, C. Raanan for histology, M. Guilliams, A. Schlitzer

and members of the Amit laboratory for fruitful discussions. We thank A. Leshem, H. Keren-Shaul, F. Sheban, L. Geirsdottir, E. Tatirovsky, F. Müller, J. Hetzer and D. Heide for technical support. A.D. is a recipient of Short-Term EMBO Fellowship no. 7395 and is supported by Eden and Steven Romick. D.P. is supported by the Helmholtz Future; Inflammation and Immunology. M.H.W. is supported by an ERC Consolidator grant (HepatoMetaboPath), an EOS grant, SFBTR179, SFBTR 209, SFBTR1335, Horizon 2020, Research Foundation Flanders under grant 30826052 (EOS Convention MODEL-IDI), Deutsche Krebshilfe projects 70113166 and 70113167, German-Israeli Cooperation in Cancer Research (DKFZ-MOST) and the Helmholtz-Gemeinschaft, Zukunftsthema 'Immunology and Inflammation' (ZT-0027). E.E. is supported by the Leona M. and Harry B. Helmsley Charitable Trust; Adelis Foundation; Pearl Welinsky Merlo Scientific Progress Research Fund; Park Avenue Charitable Fund; The Hanna and Dr. Ludwik Wallach Cancer Research Fund; Daniel Morris Trust; The Wolfson Family Charitable Trust and The Wolfson Foundation; Ben B. and Joyce E. Eisenberg Foundation; White Rose International Foundation; Estate of Malka Moskowitz; Estate of Myron H. Ackerman; Estate of Bernard Bishin for the WIS-Clalit Program; Else Kroener Fresenius Foundation; Jeanne and Joseph Nissim Center for Life Sciences Research; Aliza Moussaieff; Miel de Botton; Vainboim Family; Alex Davidoff; the V. R. Schwartz Research Fellow Chair; the Swiss Society Institute for Cancer Prevention Research at the Weizmann Institute of Science, Rehovot, Israel and by grants funded by the European Research Council; Israel Science Foundation; Israel Ministry of Science and Technology; Israel Ministry of Health; the Helmholtz Foundation; Garvan Institute; European Crohn's and Colitis Organization; Deutsch-Israelische Projektkooperation; IDSA Foundation; and Welcome Trust. E.E. is the incumbent of the Sir Marc and Lady Tania Feldmann Professorial Chair; a senior fellow, Canadian Institute of Advanced Research; and an international scholar, The Bill and Melinda Gates Foundation and Howard Hughes Medical Institute. I.A. is an Eden and Steven Romick Professorial Chair, supported by Merck KGaA, Darmstadt, Germany, the Chan Zuckerberg Initiative, the Howard Hughes Medical Institute International Scholar award, the European Research Council Consolidator Grant 724471-HemTree2.0, a Single Cell Analysis (SCA) award of the Wolfson Foundation and Family Charitable Trust, the Thompson Family Foundation, a Melanoma Research Alliance Established Investigator Award (509044), the Israel Science Foundation (703/15), the Ernest and Bonnie Beutler Research Program for Excellence in Genomic Medicine, the Helen and Martin Kimmel award for innovative investigation, the NeuroMac DFG/Transregional Collaborative Research Center Grant, an International Progressive MS Alliance/NMSS PA-1604 08459, the ISF Israel Precision Medicine Program (IPMP) 607/20 grant and an Adelis Foundation grant.

Author contributions

A.D. and I.A. designed, analyzed and interpreted all experiments. A.D. wrote the manuscript. A.D., B.L., D.A.J., I.Y., M.C., O.B., S.S.-L. and C.G. performed experiments and analyzed the data. D.P., P.R. and K.S. under supervision of M.H., and Y.S. and M.Q. under the supervision of S.R. performed experiments and analyzed the data. A. Weiner and E.D. analyzed scRNA-seq data. A.G. analyzed PIC-seq data. C.G., D.G., H.H., E.L., G.B.-Y., O.C.-E., Y.D. and M.L. recruited the patients for the study. M.S. and Z.B.-A. prepared human blood for analysis and diagnosed liver pathology. A. Weber diagnosed liver pathology. S.H. and B.M. contributed resources. A.D., E.D. and A. Weiner prepared the figures. M.H., E.E. and I.A. supervised the study.

Competing interests

The authors declare no competing interests.

Additional information

Extended data is available for this paper at https://doi.org/10.1038/s41591-021-01344-3.

Supplementary information The online version contains supplementary material available at https://doi.org/10.1038/s41591-021-01344-3.

Correspondence and requests for materials should be addressed to A.D., M.H., E.E. or I.A.

Peer review information *Nature Medicine* thanks Frank Tacke, Matteo Iannacone, Scott Friedman and the other, anonymous reviewer(s) for their contribution to the peer review of this work. Joao Monteiro was the primary editor on this article and managed its editorial process and peer review in collaboration with the rest of the editorial team.

Reprints and permissions information is available at www.nature.com/reprints.

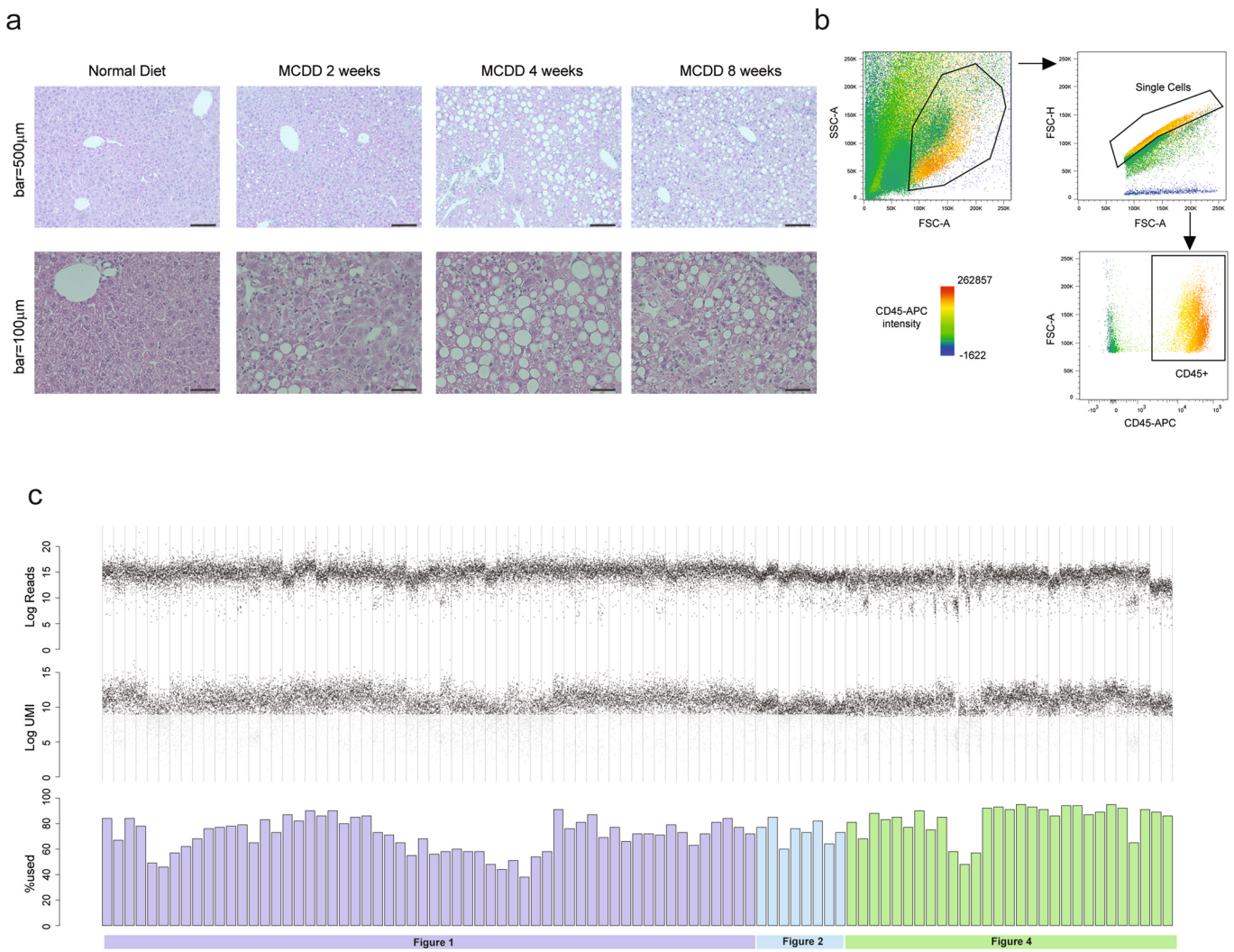

Extended Data Fig. 1 | scRNA-seq characterization of the liver immune niche during development of NASH. a, Representative pictures of H&E staining of livers in wild type C57/bl mice fed with ND or MCDD for 2, 4 and 8 weeks. **b**, Flow cytometry plots illustrating gating strategy for CD45 + immune cell selection for scRNA-seq analysis. **c**, Shown are number of reads, number of UMIs and percentage of cells analyzed per batch of 380 cells (that were pooled for library construction) for all cells collected for scRNA-seq in experiments presented in Figs. 1, 2 and 4. Black dots indicate cells used for downstream analysis and grey dots indicate cells which were filtered out.

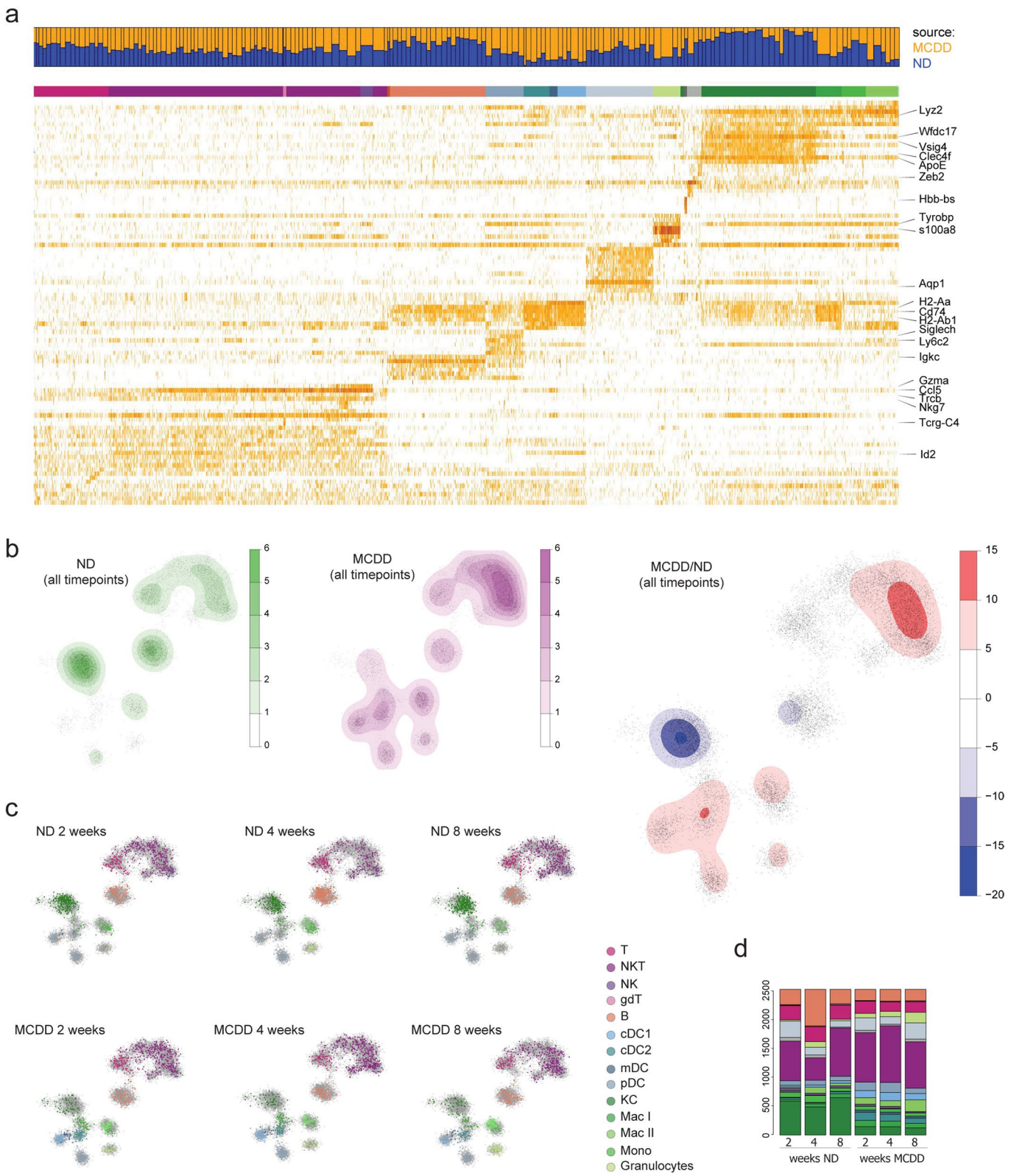

Extended Data Fig. 2 | Immune cell composition of the liver in NASH development. a, Heat map of differential gene expression for all cells colored by the assigned metacells as in Fig. 1. Top bar graph shows relative contribution of ND and MCDD liver immune cells to each metacell. **b**, Density plots depicting distribution of cells in ND and MCDD condition (downsampled to 6699 cells) and enrichment analysis of MCDD as compared to ND (all time-points analyzed together) projected on the kNN graph. Red areas represent enrichment, blue areas represent depletion. **c**, kNN graph of liver immune cells of wild-type mice kept on ND and MCDD, down-sampled to 1000 cells at each time-point analyzed. **d**, relative abundance of immune cell subtypes in livers of ND or MCDD-fed wild type mice at each analyzed time-point.

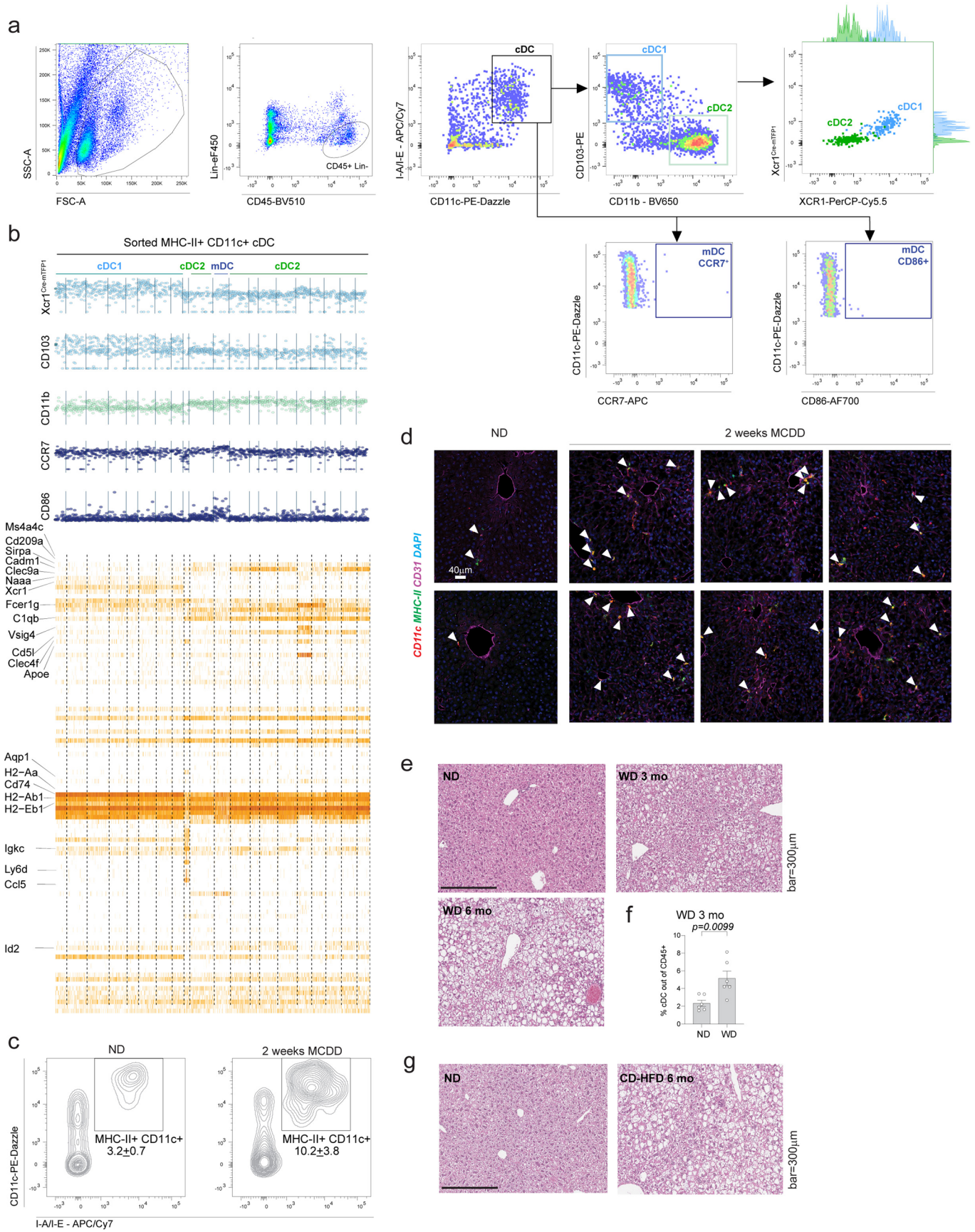

Extended Data Fig. 3 | See next page for caption.

Extended Data Fig. 3 | Hepatic cDC increase in NASH. a, Flow cytometry plots illustrating gating strategy for cDCs, cDC1, cDC2 and mDC quantification and sorting. **b**, Heat map of differential gene expression of cDC sorted from $Xcr1^{Cre\text{-}mTFP1}$ reporter mice. Top plots illustrate relative fluorescent intensity of indicated FACS markers in each cell, ordered as in the heat map. **c**, Representative flow cytometry contour-plots of CD11c + MHC-II + cells out of CD45 + Lin- gate in livers of mice fed ND or MCDD for two weeks. Population frequencies represent mean ± s.e.m. **d**, Representative immunofluorescence images of CD11c (red), MHC-II (green) and CD31 (vasculature marker; magenta) in liver section of mice fed ND or MCDD for two weeks. Cell nuclei are stained with DAPI (blue). Scale bar, 30 μm. Images representative for two independent experiments. **e**, Representative pictures of H&E staining of livers in wild type C57/bl mice fed with ND or WD for 3 and 6 months. **f**, Percentage of CD11c + MHC-II + DCs among CD45 + cells in the livers of mice fed WD for 3 months, n = 6 per group, data are presented as mean ± s.e.m.; p-value was determined by two-tailed Student's t-test. **g**, Representative pictures of H&E staining of livers in wild type C57/bl mice fed with ND or CDHFD for 6 months.

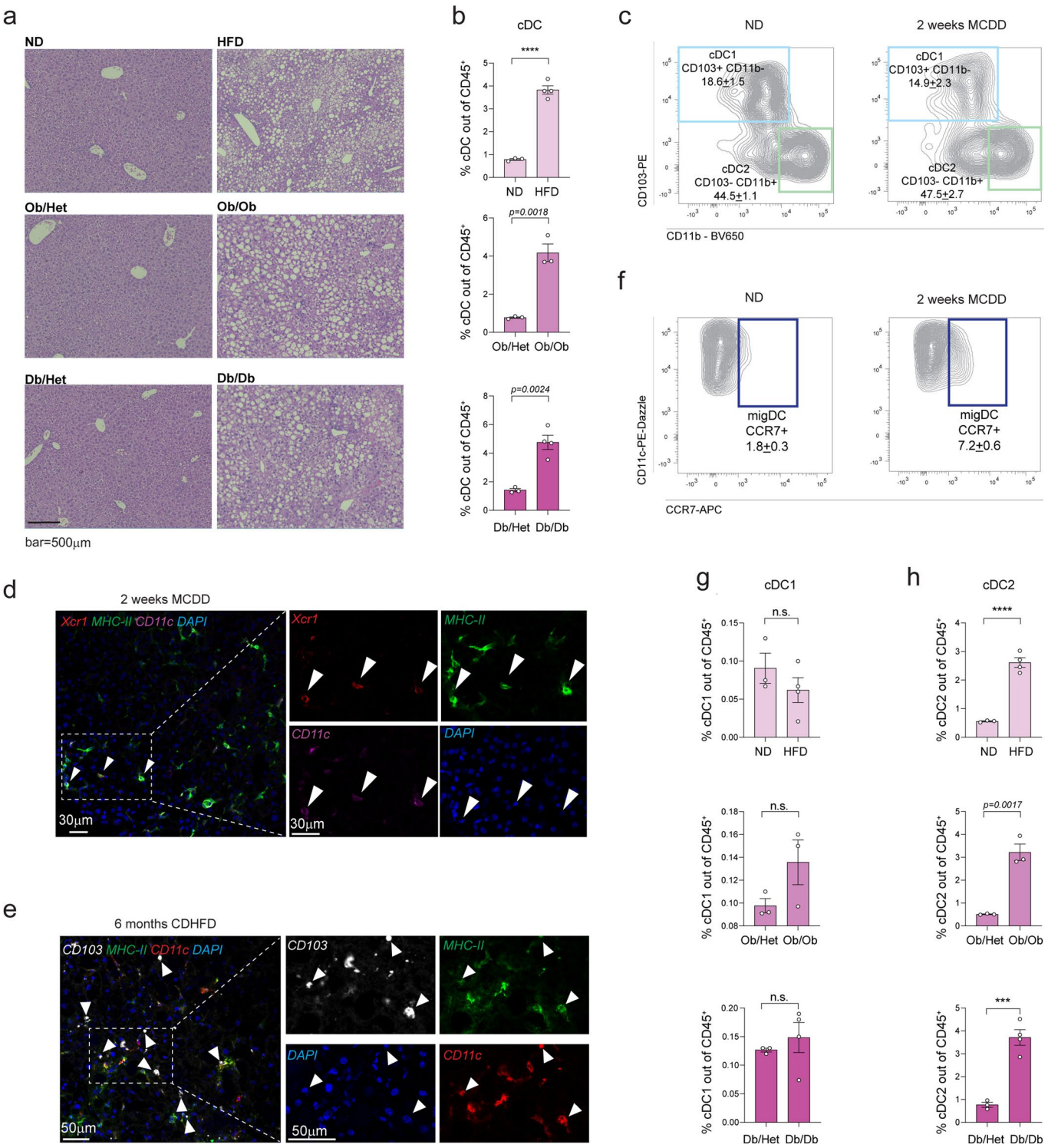

Extended Data Fig. 4 | See next page for caption.

Extended Data Fig. 4 | Proportions of hepatic cDC subtypes change in murine NASH and NAFLD models. a, Representative pictures of H&E staining of livers in wild type C57/bl mice fed with ND or HFD for 6 months, 9 week-old Ob/Ob mouse and Ob/het control, 12 week-old Db/Db mouse and Db/het control. **b**, Percentage of DCs among CD45 + cells in the livers of wild type mice fed ND or HFD for 6 months, 9 week-old Ob/Ob mouse and Ob/het control, 12 week-old Db/Db mouse and Db/het control. **c**, Representative flow cytometry contour-plots of cDC1 and cDC2 out of cDC gate in livers of mice fed ND or MCDD for two weeks. Population frequencies represent mean ± s.e.m. **d**, Representative immunofluorescence image of XCR1 (red), CD11c (magenta), MHC-II (green) and DAPI (nuclear stain, blue) in liver section of mouse fed MCDD for two weeks. Scale bar, 30 μm. Images representative for two independent experiments. **e**, Representative immunofluorescence image of CD103 (white), CD11c (red), MHC-II (green) and DAPI (nuclear stain, blue) in liver section of mouse fed CDHFD for six months. Scale bar, 50 μm. Images representative for two independent experiments. **f**, Representative flow cytometry contour-plots of CCR7 + mDCs out of cDC gate in livers of mice fed ND or MCDD for two weeks. Population frequencies represent mean ± s.e.m. **g-h**, Percentage of cDC1 (g) and cDC2 (h) among CD45 + cells in the livers of wild type mice fed ND or HFD for 6 months, 9 week-old Ob/Ob mouse and Ob/het control, 12 week-old Db/Db mouse and Db/het control. In all graphs points indicate individual mice, n = 3-4 per group. Data are presented as mean ± s.e.m.; p-values were determined by two-tailed Student's t-test; ***$p < 0.001$.

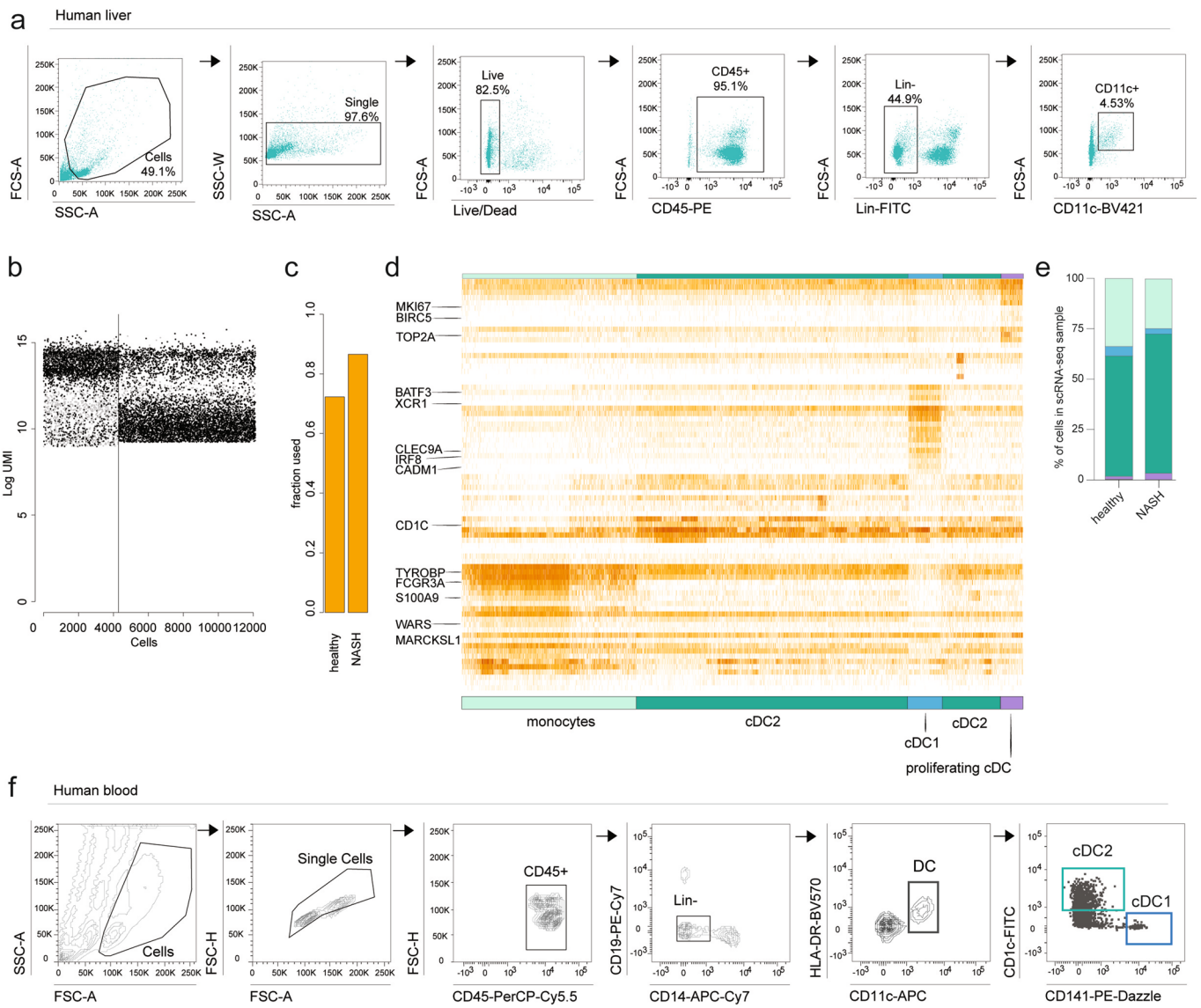

Extended Data Fig. 5 | cDC in human NASH. a, Full gating strategy used to select cDC from human livers. **b-c**, Number of UMIs (b) and percentage of QC-positive single cells (c) used for analysis out of all cells detected in scRNA-seq pipeline. **d**, Heat map of differential gene expression among CD45 + Lin-CD11C + cells sorted from healthy and NASH human livers. **e**, Relative abundance of cell subtypes among CD45 + Lin-CD11C + cells sorted from healthy and NASH human livers. **f**, Full gating strategy used to select cDC, cDC1 and cDC2 from human blood.

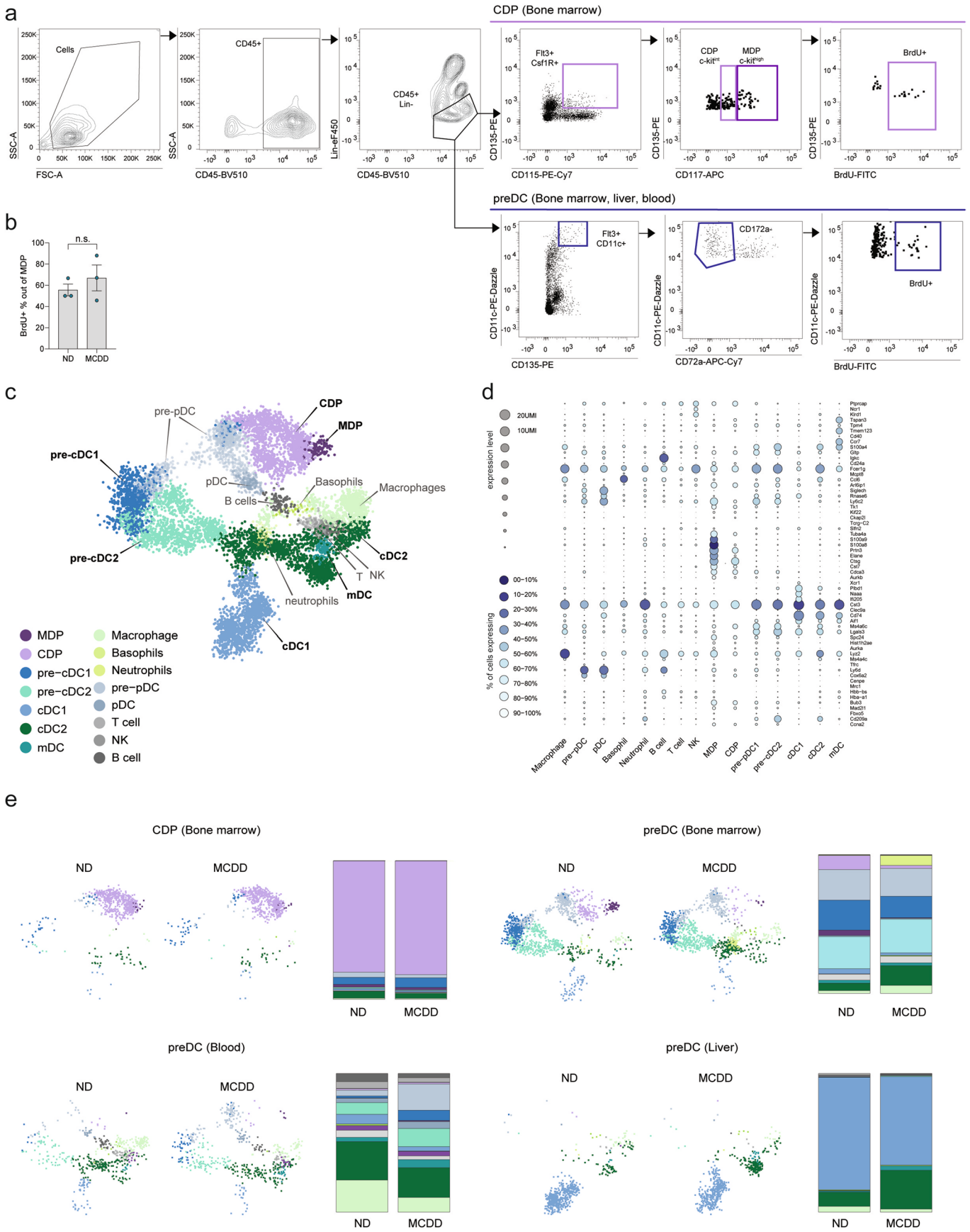

Extended Data Fig. 6 | See next page for caption.

Extended Data Fig. 6 | NASH boosts DC-poiesis. a, Flow cytometry plots illustrating gating strategy for assessing BrdU incorporation in MDP, CDPs and preDCs in the bone marrow, blood and liver. **b**, Percentage of BrdU+ cells among MDP in the bone marrow of mice fed ND or MCDD for two weeks and pulsed with BrdU 10 h prior to DC progenitor analysis. n = 3 per group, data are presented as mean ± s.e.m. **c**, kNN graph of bone marrow-isolated CDP, pre-DC isolated form the bone marrow, blood and liver and liver DC isolated from wild-type mice kept on ND or fed MCDD for two weeks. **d**, Plot representing expression of marker genes in annotated clusters in cells showed in c. Color intensity indicates log2 of the mean UMI count; circle size represents percentage of cells within cluster expressing indicated genes. **e**, kNN graphs showing distribution of single cells from different organs and diet-regiments matched with bar plots showing relative contribution of each annotated cell type among CDP sorted from the bone marrow and pre-DCs sorted from the bone marrow, blood and liver of wild-type mice kept on ND or on MCDD for two weeks. Plots were down-sampled to 680 cells for CDP, 1404 for bone marrow preDC, 601 for blood preDC and 622 for liver preDC.

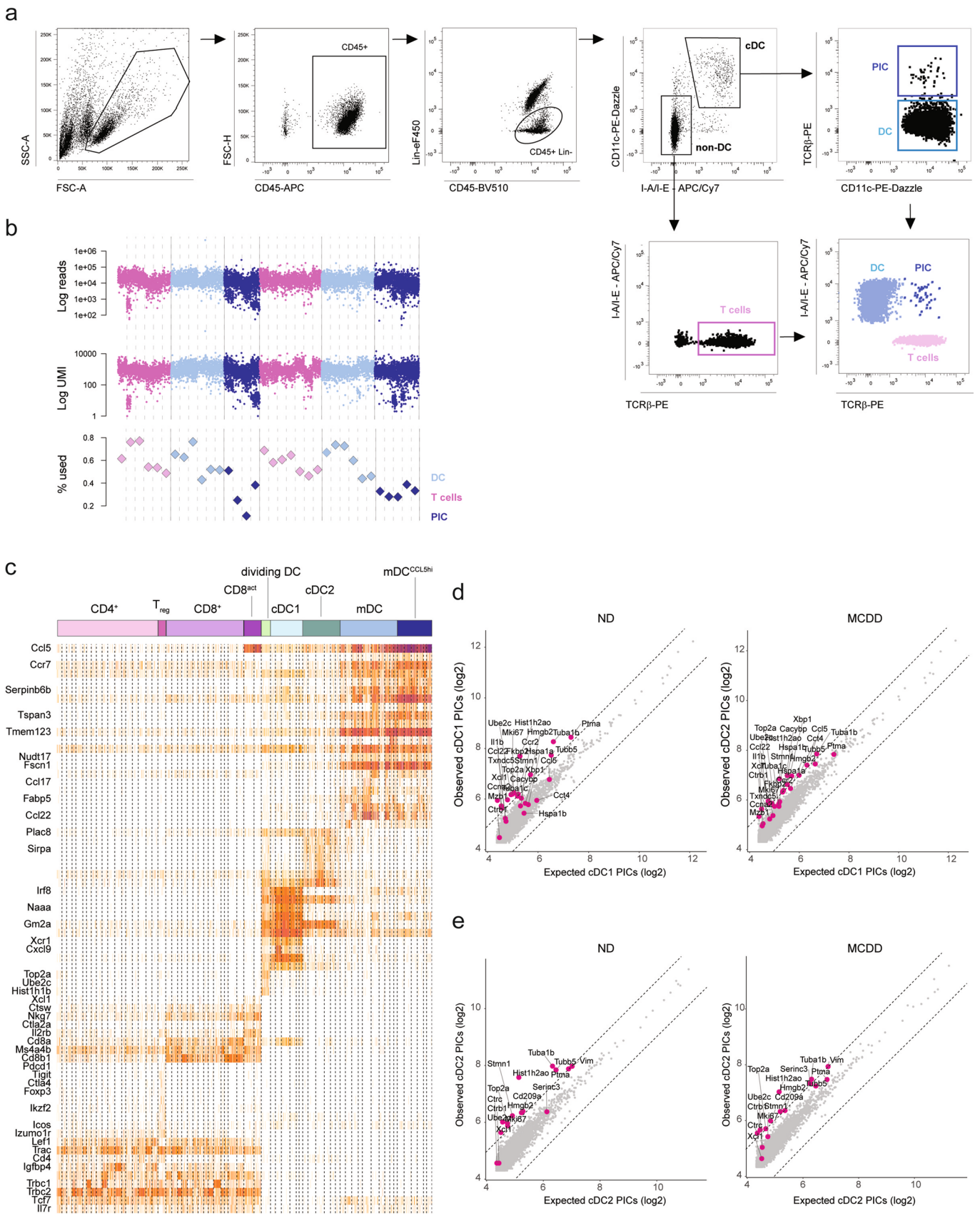

Extended Data Fig. 7 | See next page for caption.

Extended Data Fig. 7 | Characterization of genetic signatures of DC-T pairs in liver lymph nodes in NASH. a, Full gating strategy for T and DC, as well as PIC-sorting from murine liver lymph nodes. **b**, Number of reads, number of UMIs and percentage of cells analyzed per batch of 380 cells (that were pooled for library construction) in PIC-seq experiments. **c**, Heat map of differential gene expression for all single cells sorted as DC and T cells, annotated based on their gene expression, and used to create 'expected PICs' for PIC-seq analysis. Highlighted are marker genes for the annotated DC and T subtypes. **d,e**, Gene-expression levels in observed PICs assigned to the cDC1-T identity (d) or cDC2-T identity (e), plotted against their expected levels as determined by PICseq in the liver lymph nodes of mice kept on ND or MCDD for two weeks. Highlighted genes are expressed differentially between observed and expected PICs in one or both conditions.

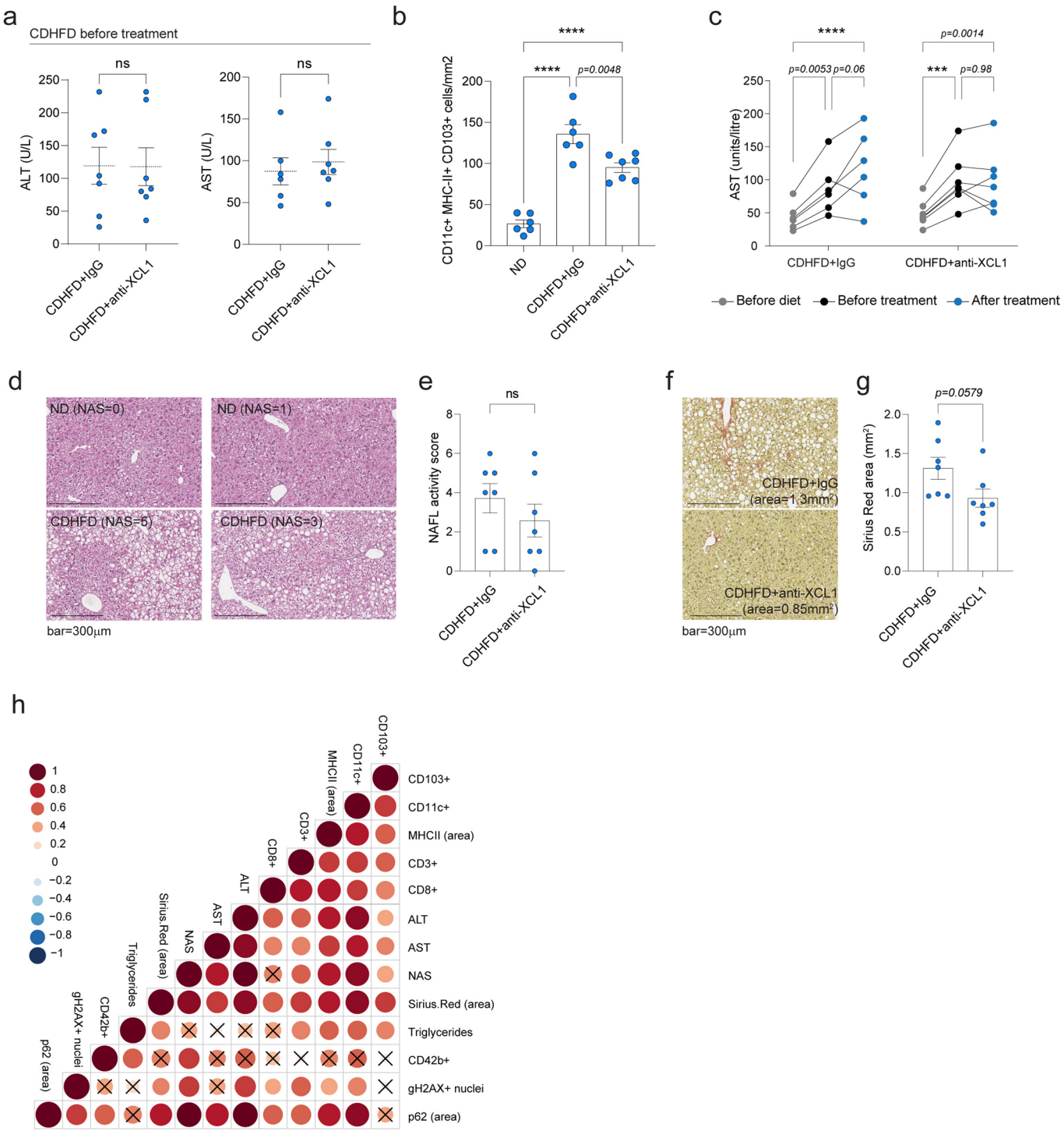

Extended Data Fig. 8 | Partial depletion of hepatic cDC1 infiltration using anti-XCL1 antibody in CDHFD-fed mice attenuates NASH progression. a, Levels of liver enzymes ALT and AST in the serum of wild type CDHFD-fed mice before anti-XCL1 or IgG isotype control treatment. **b**, Quantification of CD103 + MHC-II + CD11c + cells from 5-10 randomly selected areas per mouse **c**, Levels of AST, a measure of tissue injury, including liver, in the serum of wild type mice before feeding with CDHFD (grey), after 5 months of CDHFD but before treatment (black), and following 4 weeks of anti-XCL1 or control IgG treatment (blue). In a-c n = 6-7 per group. Data are presented as mean ± s.e.m. P-values were determined by two-way ANOVA with Tukey's multiple comparisons test; ***$p < 0.001$, ****$p < 0.0001$ **d,e**, Representative pictures of H&E staining (d) and pathological evaluation of NAFLD activity score (e) in anti-XCL1 or IgG isotype control-treated, CDHFD-fed mice. Images representative for two experiments. **f,g**, Representative pictures (f) and quantification (g) of Sirius Red staining in anti-XCL1 or IgG isotype control-treated, CDHFD-fed mice. Images representative for two independent experiments. In e, g, data are presented as mean ± s.e.m.; n = 7 per group, two-tailed Student's t-test h. Correlation analysis between MHC-II$^+$CD11c$^+$CD103$^+$ cDC1 count and NASH pathology parameters in anti-XCL1-treated and IgG-treated mice. n = 14 mice, two-tailed Spearman correlation (crossed out points $p > 0.05$; color and circle size indicate R2).

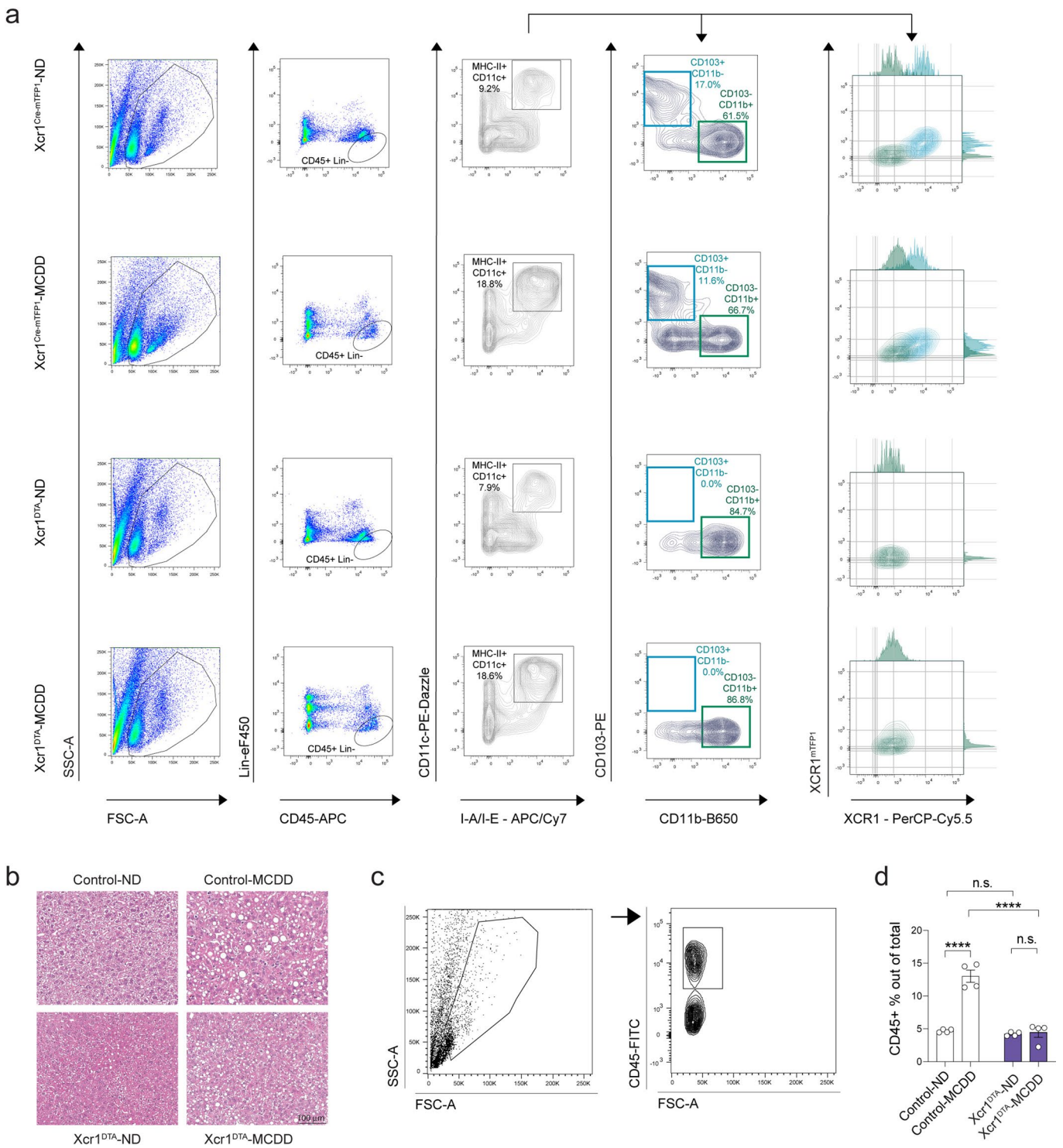

Extended Data Fig. 9 | Depletion of cDC1 in Xcr1DTA mice prevents NASH-induced immune infiltration. a, Flow cytometry plots illustrating specific depletion of cDC1 in Xcr1DTA mice, compared to control mice kept both on ND and after two week of MCDD feeding. **b**, Representative pictures of H&E staining control mice and Xcr1DTA mice (lacking Xcr1+cDC1) fed with ND or MCDD for two weeks. Images representative for two independent experiments. **c,d**, FACS gating strategy and quantification of CD45+immune cell percentage among all cells isolated from livers of control and Xcr1DTA mice kept on ND or MCDD for two weeks. n = 4 per group. Data are presented as mean ± s.e.m.; ****$p < 0.0001$ by One-way ANOVA with Tukey's multiple comparisons test.

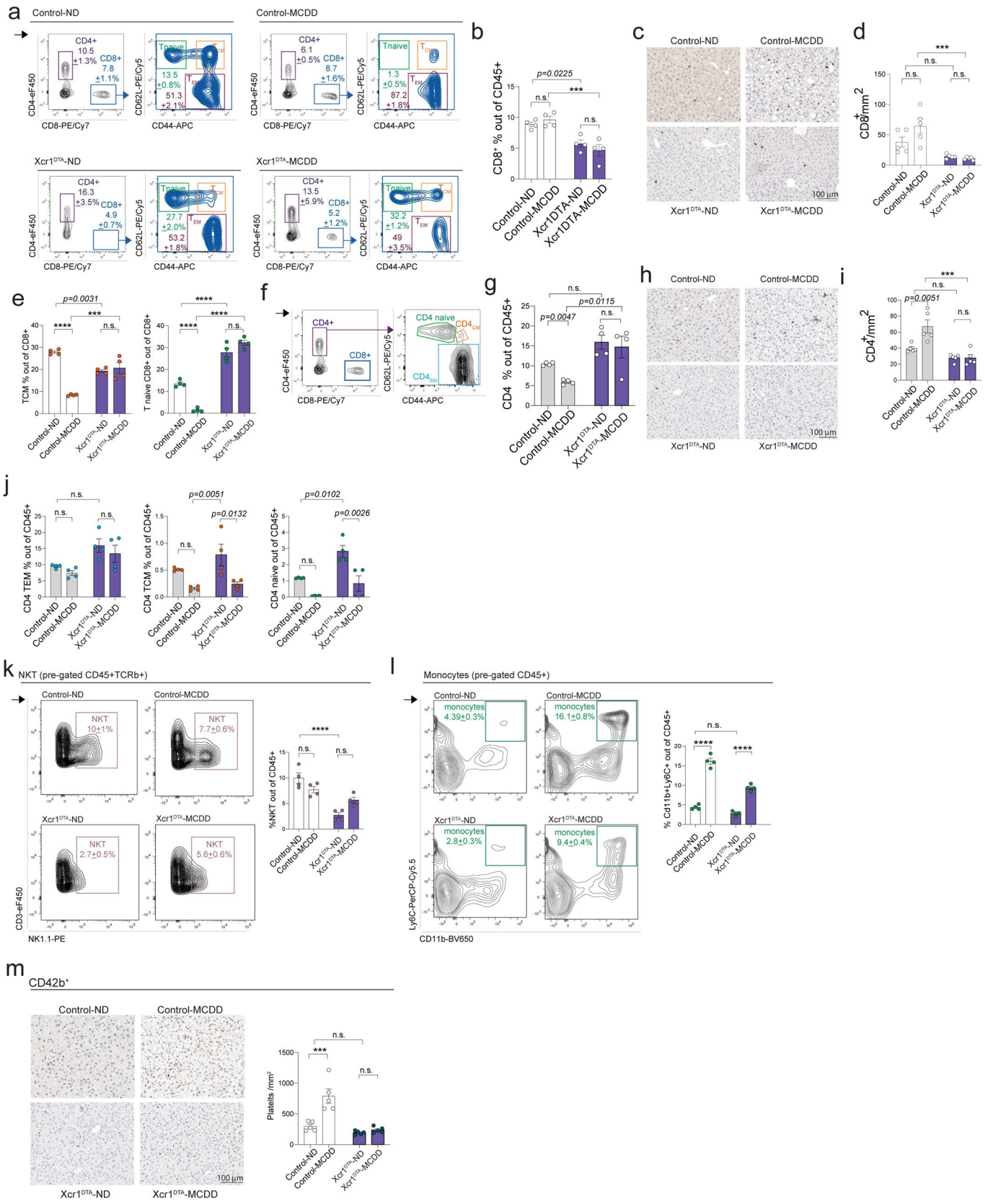

Extended Data Fig. 10 | See next page for caption.

Extended Data Fig. 10 | cDC1 modulate hepatic immune cell populations in the MCDD model of NASH. a,b, Representative flow cytometry plots (a) and flow cytometry-based quantification (b) of CD8 + cells in the livers of control and Xcr1DTA mice kept on ND or MCDD for two weeks. n = 4 per group. **c,d**, Representative microscopic images of IHC staining for CD8 (c), and image-based quantification (d) of the stained CD8 + cells in the livers of control and Xcr1DTA mice kept on ND or MCDD for two weeks. bar=100 μm. For quantification 5–10 randomly selected fields per mouse were averaged, n = 5 mice in control and Xcr1DTA-ND groups, n = 4 in the Xcr1DTA-MCDD group. **e**, FACS-based quantification of CD44 + CD62L + T central memory CD8 + T cells and naïve CD44-CD8 + T cells, separated as shown in (a) in the livers of control and Xcr1DTA mice kept on ND or MCDD for two weeks. n = 4 individual mice per group **f**, Flow cytometry plots representing gating strategy used to dissect CD4 + T cell subpopulations. **g**, Flow cytometry-based quantification of CD4 + T cell percentage among CD45 + immune cells in the livers of control and Xcr1DTA mice kept on ND or MCDD for two weeks. n = 4 mice per group **h,i**, Representative microscopic images of IHC staining for CD4 (h) and image based quantification (i) of CD4 + cells in the livers of control and Xcr1DTA mice kept on ND or MCDD for two weeks. bar = 100 μm. For quantification 5–10 randomly selected fields per mouse were averaged, n = 5 mice per group. **j**, Flow cytometry-based quantification of CD4 + T cell subsets in the livers of control and Xcr1DTA mice kept on ND or MCDD for two weeks. n = 4 mice per group **k,l**, Flow cytometry contour plots and flow cytometry-based quantification of NKT cells (k) and monocytes (l) in the livers of control and Xcr1DTA mice kept on ND or MCDD for two weeks. n = 4 mice per group **m,** Representative microscopic images of IHC staining for CD42b, a marker of platelets, and image based quantification of the stained cells in the livers of control and Xcr1DTA mice kept on ND or MCDD for two weeks. bar = 100 μm. For quantification 5–10 randomly selected fields per mouse were averaged, n = 5 mice per group. In all graphs data are presented as mean ± s.e.m. P-values were determined by one-way ANOVA with Tukey's multiple comparisons test; ***$p < 0.001$, ****$p < 0.0001$.

nature research

Corresponding author(s): Aleksandra Deczkowska, Mathias Heikenwälder, Eran Elinav, Ido Amit NMED-A105989

Last updated by author(s): Mar 30, 2021

Reporting Summary

Nature Research wishes to improve the reproducibility of the work that we publish. This form provides structure for consistency and transparency in reporting. For further information on Nature Research policies, see our Editorial Policies and the Editorial Policy Checklist.

Statistics

For all statistical analyses, confirm that the following items are present in the figure legend, table legend, main text, or Methods section.

n/a	Confirmed	
☐	☒	The exact sample size (*n*) for each experimental group/condition, given as a discrete number and unit of measurement
☐	☒	A statement on whether measurements were taken from distinct samples or whether the same sample was measured repeatedly
☐	☒	The statistical test(s) used AND whether they are one- or two-sided *Only common tests should be described solely by name; describe more complex techniques in the Methods section.*
☐	☒	A description of all covariates tested
☐	☒	A description of any assumptions or corrections, such as tests of normality and adjustment for multiple comparisons
☐	☒	A full description of the statistical parameters including central tendency (e.g. means) or other basic estimates (e.g. regression coefficient) AND variation (e.g. standard deviation) or associated estimates of uncertainty (e.g. confidence intervals)
☐	☒	For null hypothesis testing, the test statistic (e.g. *F*, *t*, *r*) with confidence intervals, effect sizes, degrees of freedom and *P* value noted *Give P values as exact values whenever suitable.*
☒	☐	For Bayesian analysis, information on the choice of priors and Markov chain Monte Carlo settings
☒	☐	For hierarchical and complex designs, identification of the appropriate level for tests and full reporting of outcomes
☐	☒	Estimates of effect sizes (e.g. Cohen's *d*, Pearson's *r*), indicating how they were calculated

Our web collection on statistics for biologists contains articles on many of the points above.

Software and code

Policy information about availability of computer code

Data collection: Quantitative data were collected primarily into Microsoft excel.

Data analysis	For scRNA-seq analysis For MARS-seq, demultiplexing and filtering was performed as previously described (DOI: 10.1038/s41596-019-0164-4), with the following adaptations. Mapping of reads was performed using HISAT (version 0.1.6); reads with multiple mapping positions were excluded. Reads were associated with genes if they were mapped to an exon, using the Ensembl gene annotation database (EMBL release 90). The level of spurious unique molecular identifiers (UMIs) in the data were estimated by using statistics on empty MARS-seq wells. For both MARS-seq and 10x, cells with fewer than 500 UMIs or more than 20% mitochondrial genes or mitochondrial genes being the most differential were discarded from the analysis. For PIC-seq, cell with fewer than 1000 UMIs were discarded. All downstream analysis was performed in R (version R-4.0.4). The metacell pipeline (https://github.com/tanaylab/metacell) was used to derive informative genes and compute cell-to-cell similarity, to compute K-nn graph covers and derive distribution of RNA in cohesive groups of cells (or metacells), and to derive strongly separated clusters using bootstrap analysis and computation of graph covers on resampled data. We removed specific mitochondrial genes, immunoglobulin genes, and genes linked with poorly supported transcriptional models (annotated with the prefix ''Rp-''). Gene features were selected using the parameter Tvm = 0.3 and a minimum total UMI count > 50. We subsequently performed hierarchical clustering of the correlation matrix between metacells and grouped them into clusters representing cell types and states. We used K = 100, 500 bootstrap iterations and otherwise standard parameters. All downstream analyses were performed in R (version R-4.0.4). PIC-seq (https://github.com/aygoldberg/PIC-seq) was used for PIC-seq analysis (Fig.5). Graphs for non-scRNA-seq analyses were created using GraphPad Prism 8. Graohs correlating cDC1 cell abundance with liver pathology correlation graphs were created in R (version R-4.0.4). Flow cytometry was analyzed using BD FACS-Diva software BD FACSDiva software v.9.0 (BD Bioscience) and FlowJo software v.10.7.1 (FlowJo, LLC). Immunofluorescent Images were acquired and processed with the same threshold settings across samples using Imaris 9.7 (Bitplane). Non-fluorescent images were analysed using Aperio Image Scope software 12.4.0.

For manuscripts utilizing custom algorithms or software that are central to the research but not yet described in published literature, software must be made available to editors and reviewers. We strongly encourage code deposition in a community repository (e.g. GitHub). See the Nature Research guidelines for submitting code & software for further information.

Data

Policy information about availability of data

All manuscripts must include a data availability statement. This statement should provide the following information, where applicable:

- Accession codes, unique identifiers, or web links for publicly available datasets
- A list of figures that have associated raw data
- A description of any restrictions on data availability

The scRNA-seq datasets generated and analyzed in this manuscript are available at GEO submission GSE169447.

Field-specific reporting

Please select the one below that is the best fit for your research. If you are not sure, read the appropriate sections before making your selection.

☒ Life sciences ☐ Behavioural & social sciences ☐ Ecological, evolutionary & environmental sciences

For a reference copy of the document with all sections, see nature.com/documents/nr-reporting-summary-flat.pdf

Life sciences study design

All studies must disclose on these points even when the disclosure is negative.

Sample size	pilot experiments and previously published results were used to estimate the samples size such that appropriate statistical tests would yiled significant results (DOI: 10.1016/j.cell.2019.05.054, DOI: 10.1038/s41586-021-03362-0). the exact n numbers are indicated in figure legends.
Data exclusions	in scRNA-seq analysis, cells which failed to pass quality control (min 500 UMIs, 1000UMIs for the PIC-seq experiments) were excluded. Cells which passed the QC in scRNA-seq experiment in Fig. 1 but were annotated as non-immune (hepatocytes, epithelial), were also excluded from final analysis.
Replication	Main findings from the scRNA-seq experiments, except PIC-seq, were confirmed using other methods. PIC-seq experiment was performed in three independent repetitions. All non-scRNA-seq experiments were replicated at least twice, except if the experiment's goal was to confirm previously observed phenotypes, such as H&E staining in fig. 3d, 3g, 4a, confirming previous findings as reported e.g. DOI: 10.1038/s41586-021-03362-0, 10.1002/hep.21655, 10.1038/emm.2016.123, 10.4196/kjpp.2014.18.4.333.). All attempts of replication were successful.
Randomization	Mice (littermates, sorted according to their genotypes) were allocated to diet regiments at random. In fig 6, CDHFD were assigned to anti-XCL1 and IgG groups following the evaluation of ALT/ASP activity in their sera (Extended data fig. 8a). For human liver samples groups were allocated based on pathology (NAS-score) in H&E staining, which was evaluated by an experienced liver pathologist (Prof. Dr. Achim Weber, University of Zürich). For human blood samples the diagnosis of NAFLD was based on ultrasound evaluation and NASH diagnosis was based on the presence of ballooning, steatohepatitis and fibrosis on liver biopsy, when it was available, or on the presence of fibrosis by noninvasive liver assessment. These evaluations were performed by experienced doctors in the Chaim Sheba Tel-Hashomer Liver Diseases Center.
Blinding	in mouse experiments and human analysis the experimenter was using a running sample number and was blinded to the genotype, treatment, or classification based on phenotype (human NAFLD/NASH) during the experiment.

Reporting for specific materials, systems and methods

We require information from authors about some types of materials, experimental systems and methods used in many studies. Here, indicate whether each material, system or method listed is relevant to your study. If you are not sure if a list item applies to your research, read the appropriate section before selecting a response.

Materials & experimental systems

n/a	Involved in the study
☐	☒ Antibodies
☒	☐ Eukaryotic cell lines
☒	☐ Palaeontology and archaeology
☐	☒ Animals and other organisms
☐	☒ Human research participants
☒	☐ Clinical data
☒	☐ Dual use research of concern

Methods

n/a	Involved in the study
☒	☐ ChIP-seq
☐	☒ Flow cytometry
☒	☐ MRI-based neuroimaging

Antibodies

Antibodies used

For marker-based validations and sorting of specific DC and DC progenitor populations, mouse samples were stained using the following antibodies. PE-Dazzle-conjugated CD45 (1:1000; Biolegend, clone 30-F11) or FITC-conjugated CD45 (1:100; eBioscience, clone 30-F11) marking leukocytes. eFluor450-conjugated CD3 (eBioscience; 1:50; clone 17A2), CD19 (eBioscience; 1:150; clone 1D3), B220 (eBioscience; 1:150; clone RA3-6B2), NK1.1 (eBioscience; 1:150; clone: PK136), Ly6G (eBioscience; 1:150; clone 1A8) and Ter119 (eBioscience; 1:150; clone TER-119) to exclude T, B, NK, neutrophils and erythrocytes. PE or PE-Dazzle-conjugated CD11c (clone N418), FITC- or APC-Cy7 conjugated I-A/I-E (Biolegend; 1:150; clone M5/114.15.2), Brilliant Violet 650-conjugated CD11b (Biolegend; 1:200; clone M1/70), PE-conjugated CD103 (Biolegend; 1:200; clone 2E7), APC-conjugated XCR1 (Biolegend; 1:20; clone ZET), APC-conjugated CCR7 (Biolegend; 1:20; clone 4B12), PE/Cy7-conjugated CD83 (Biolegend; 1:20; clone Michel-19), PE-conjugated CD135 (FLT3; eBioscience; 1:150; clone A2F10), PE-Cy7- or PE-conjugated CD115 (eBioscience; 1:150; clone AFS98), APC/Cy7-conjugated Ly6C (Biolegend; 1:200; clone HK1.4), APC/Cy7- conjugated c-kit (Biolegend;1:100; clone 2B8) and DAPI (in the same channel with Lineage staining), for live/dead cell detection.
For T cell analysis and PICs sorting, the following antibodies were used: PE-Dazzle-conjugated CD45 (1:1000; Biolegend, clone 30-F11) or FITC-conjugated CD45 (1:100; eBioscience, clone 30-F11), PE-Dazzle or PE-conjugated CD11c (Biolegend; 1:200; clone N418), FITC- or APC-Cy7 conjugated I-A/I-E (Biolegend; 1:150; clone M5/114.15.2), FITC-conjugated TCRbeta (Biolegend; 1:50; clone H57-597) or PE-conjugated TCRbeta (Biolegend; 1:200; clone H57-597), eFluor450-conjugated CD4 (eBioscience; 1:100;clone GK1.5), PE-Cy7-conjugated CD8 (Biolegend; 1:100; clone 53-6.7), PE-Cy5-conjugated CD62L (Biolegend; 1:100; clone DREG-56), APC-conjugated CD44 (Biolegend; 1:50; clone IM7).
For NKT cell analysis, FITC-conjugated CD45 (1:100; eBioscience, clone 30-F11), eFluor450-conjugated CD3 (eBioscience; 1:50; clone 17A2), PE-conjugated NK1.1 (eBioscience; 1:200; clone PK.126) were used. For monocyte analysis: FITC-conjugated CD45 (1:100; eBioscience, clone 30-F11), PerCP-Cy5.5 conjugated Ly6C (Biolegend; 1:200; clone HK1.4), and Brilliant Violet 650-conjugated CD11b (Biolegend; 1:200; clone M1/70).
For human blood DC analysis, the following antibodies were used: PerCP-Cy5.5-conjugated CD45 (1:20; Biolegend; clone H130), FITC-conjugated CD1c (1:20; Biolegend; clone L161), APC-conjugated CD11c (1:5; BD Bioscience; clone B-ly6), APC/Cy7-conjugated CD14 (1:20; BD Bioscience; clone MOPg), BV570-conjugated HLA-DR (1:20; Biolegend; clone L243), PE-Dazzle-conjugated CD141 (1:20; Biolegend; clone M80), PE/Cy7-conjugated CD19 (1:20; Beckman Coulter; clone J3-119).
For human DC sorting from the liver, the following antibodies were used: PE-conjugated CD45 (1:20; Biolegend; clone H130), FITC-conjugated Anti-Human Lineage Cocktail 3 (lin 3; including anti-CD3, anti-CD14, anti-CD19 and anti-CD20; BD Biosciences cat. 643510, according to the manufacturer's guidelines), BV421-conjugated CD11c (1:20; Biolegend clone 3.9) along with the live dead stain (Thermofischer, L34973).
For neutralization of XCL1, 50µg of anti-XCL1 antibodies (R&D systems MAB486) or of isotype-matched control antibodies (R&D systems MAB006) were injected i.p. twice a week for 4 weeks (total of 8 injections).

Validation

Validation of commercial antibodies was done by regular quality control of each lot by the manufacturer (e.g. Biolegend "The antibody was purified by affinity chromatography and conjugated with PE under optimal conditions.";"Each lot of this antibody is quality control tested by immunofluorescent stainign with flow cytometric analysis."; "Every lot of product is quality tested against the "gold standard" reference lot. A new lot is only released based on our defined QC specifications to ensure lot to lot reproducibility and reliability. Biolegend guarantees the stability and performance of all our products shipped at room temperature.")

Animals and other organisms

Policy information about studies involving animals; ARRIVE guidelines recommended for reporting animal research

Laboratory animals

mice, both male and female, 8-24 weeks old. Strains used: C57bl/6, Ob/ob, Db/db, Xcr1Cre-mTFP147 and DTA+/+(B6.129P2-Gt(ROSA)26Sortm1(DTA)Lky/J).

Wild animals

study did not involve wild animals

Field-collected samples

study did not involve field collected samples

Ethics oversight	All experimental procedures were performed in accordance to Institutional Animal Care and Use Committee (IACUC) of the Weizmann Institute of Science and German Law (G141/19).

Note that full information on the approval of the study protocol must also be provided in the manuscript.

Human research participants

Policy information about studies involving human research participants

Population characteristics	Blood samples were drawn from patients with chronic liver disease that were recruited at Chaim Sheba Tel-Hashomer Liver Diseases Center. The group included both male and female patients, average age was 50. Human liver tissue samples were collected from patients undergoing bariatric surgery at the Department of Surgery at Heidelberg University Hospital. The group included both male and female patients, average age was 50. Liver sections were stained for HE in the division of Chronic Inflammation and Cancer, DKFZ, and NAS-score was evaluated by an experienced liver pathologist (Prof. Dr. Achim Weber, University Zürich).
Recruitment	Patients with chronic liver disease registered at Chaim Sheba Tel-Hashomer Liver Diseases Center. The patients were recruited by the physicians in the Liver Disease Center In the Chaim Sheba Medical Center. Chaim Sheba is the largest governmental hospital in Israel. Therefore, patients from all over Israel can come to the Liver Disease Center. No self selection bias was taken into consideration. Prior to patient inclusion, written informed consent was obtained. The diagnosis of NAFLD was based on ultrasound evaluation. NASH diagnosis was based on the presence of ballooning, steatohepatitis and fibrosis on liver biopsy, when it was available, or on the presence of fibrosis by noninvasive liver assessment. Liver biopsies were collected from patients undergoing bariatric surgery at the Department of Surgery at Heidelberg University Hospital, and the selection of the two groups was performed later, on the basis of the liver histology (NAS-score) diagnosed by an experienced pathologist independently on the BMI. We did not considered any other biases (e.g. age, sex, co-morbidities...) that would affect the results in the selection of the two groups.
Ethics oversight	For the human blood analysis, the protocol was approved by the institutional review board of the Chaim Sheba Medical Center. For the human liver study institutional review board approval was obtained from the Medical Ethics Committee of Heidelberg University (reference number S-629/2013) headed by Prof. Thomas Strowitzki (full committee http://www.medizinische-fakultaet-hd.uni-heidelberg.de/Mitglieder.108623.0.html). All patients had previously signed the corresponding institutional review board-approved consent forms.

Note that full information on the approval of the study protocol must also be provided in the manuscript.

Flow Cytometry

Plots

Confirm that:

☒ The axis labels state the marker and fluorochrome used (e.g. CD4-FITC).

☒ The axis scales are clearly visible. Include numbers along axes only for bottom left plot of group (a 'group' is an analysis of identical markers).

☒ All plots are contour plots with outliers or pseudocolor plots.

☒ A numerical value for number of cells or percentage (with statistics) is provided.

Methodology

Sample preparation	Mice were fasted for 14h and anaesthetized with an intraperitoneal injection of a ketamine (100mg kg−1) and xylazine (10 mg kg−1) mixture. Liver leukocytes were isolated by a modification of the two-step collagenase perfusion method of Seglen Digestion using Liberase™ TL (cat. no. 5401020001; Roche) for scRNA-seq, or using The Liver Dissociation Kit (Miltenyi Biotec, cat. no. 130-105-807) according to the manufacturer's guidelines for FACS analyses. Bone marrow was isolated by flushing from tibia and femur. Cervical, celiac and portal lymph nodes were processed for recovery of DC-T PICs and single DC and T cells as previously described48. Briefly, lymph nodes were digested in Isocove's modified Dulbecco's medium (Sigma-Aldrich) medium supplemented with Liberase-TL (100µgml−1, Roche) and DNase I (100µgml−1, Roche) at 37°C for 20min and dissociated with 18G and 21G needle. Blood was collected from the heart. Red cell lysis was performed on bone marrow and blood samples (RBC Lysis Buffer, Invitrogen). Isolated leukocytes stained cell surface markers for flow cytometry analysis and sorting. Cell populations were sorted using either SORP-aria (BD Biosciences) or ARIA-III instrument (BD Biosciences), and analyzed using BD FACSDIVA software (BD Biosciences) and FlowJo software. Immune cells in Fig.1 were sorted as Cells -> singlets -> DAPI- ->CD45+ cDC in Extended data Fig.3a were sorted as Cells-> singlets -> ->CD45+ ->DAPI-Lin- ->MCH-IIhiCD11chi, cDC1 were gated as Cells-> singlets -> ->CD45+ ->DAPI-Lin- -> MCH-IIhiCD11chi -> CD103+XCR1+CD11b-, cDC2 were gated as Cells-> singlets -> ->CD45+ ->DAPI-Lin- -> MCH-IIhiCD11chi -> CD103-XCR1-CD11b+. mDC were gated as Cells-> singlets -> ->CD45+ ->DAPI-Lin- -> MCH-IIhiCD11chi -> CD86+/CCR7+ CDP (Fig.4, Extended data fig.6a) were selected as: cells -> singlets -> CD45+ -> Lin− -> CD135+CSF−1R+ -> CD117int -> BrdU+ preDC (Fig.4, Extended data fig.6a) were selected as: cells -> singlets -> CD45+ -> Lin− -> CD135+CD11c+ -> CD172- -> BrdU+ T cells (Fig 5, Extended data fig.7) were selected as: cells -> CD45+ -> Lin− -> CD11c-MHC-II- -> TCRb+ PICS (Fig 5, Extended data fig.7) were selected as: cells -> CD45+ -> Lin− -> CD11c+MHC-II+ -> TCRb+ CD8+ T cell subsets (Fig 6, Extended data fig.10) were selected as: cells -> singlets -> CD45+ -> Lin− -> CD11c+MHC-II+ -> CD8+ -> CD44+CD62L+(central memory)/ CD44+CD62L-(effector memory)/ CD44-CD62L+(naive)

CD4+ T cell subsets (Fig 6, Extended data fig.10) were selected as: cells -> singlets -> CD45+ -> Lin− -> CD11c+MHC-II+ -> CD4 + -> CD44+CD62L+(central memory)/ CD44+CD62L-(effector memory)/ CD44-CD62L+(naive)
Monocytes (Fig 6, Extended data fig.10) were selected as: cells -> singlets -> CD45+ -> CD11b+Ly6c+
NK (Fig 6, Extended data fig.10) were selected as: cells -> singlets -> CD45+ -> TCRb+-> NK1.1+

Peripheral blood from human patients was collected to EDTA-containing tubes (Becton Dickinson). Each sample was diluted 1:1 in ice cold FACS buffer. Mononuclear cell separation was performed by density centrifugation media (Ficoll-Paque; GE Healthcare Life Sciences) in a 1:1 ratio with diluted blood cells. Centrifugation (460g, 25min) was performed at 10°C, and the mononuclear cells were carefully aspirated and washed with ice-cold FACS buffer. After red blood cell lysis (Sigma-Aldrich) for 5min at 4°C and washing cells were frozen in 10% DMSO in FBS and stored at -80°C until further processing. On the day of the analysis, the cells were washed twice with FACS buffer, stained and analyzed using BD FACSDIVA software (BD Bioscience) and FlowJo software (FlowJo, LLC).
cDCs in human blood (Fig.3f-i, Extended data fig.5f) Cells -> single -> CD45+ -> Lin- -> CD11c+HLA-DR+. cDC1 were selected as CD1c-CD141+. cDC2 were selected as CD1c+CD141-.
Liver biopsies from bariatric surgery patients were collected in RPMI (Supplemented with 10%FBS) and immediately transported on ice to the laboratory. A section of tissue was formalin fixed for histopathological evaluation; however, the bulk of the tissue was digested using Miltenyi Tumor dissociation Kit (cat no. 130-095-929) as per the manufacturer's instructions. Single cell suspensions thus generated were stored in Liquid nitrogen in FBS+20% DMSO until further processing. For sorting and single cell RNAseq of DCs obtained from control and NASH livers, the stored cells were thawed in a 37oC water bath, washed once with complete media and once with FACS buffer (PBS+2% FBS). After FC blocking, cells were stained in dark for 30 min and washed once with FACS buffer and once with sorting buffer (PBS+0.5mM EDTA).
cDCs in human liver (Fig.3a,b, Extended data fig.6a) were gated Cells -> single -> live -> CD45+ -> Lin- -> CD11c+
Mice were fasted for 14h and anaesthetized with an intraperitoneal injection of a ketamine (100mg kg−1) and xylazine (10 mg kg−1) mixture. Liver leukocytes were isolated by a modification of the two-step collagenase perfusion method of Seglen Digestion using Liberase™ TL (cat. no. 5401020001; Roche) for scRNA-seq, or using The Liver Dissociation Kit (Miltenyi Biotec, cat. no. 130-105-807) according to the manufacturer's guidelines for FACS analyses. Bone marrow was isolated by flushing from tibia and femur. Cervical, celiac and portal lymph nodes were processed for recovery of DC-T PICs and single DC and T cells as previously described48. Briefly, lymph nodes were digested in Isocove's modified Dulbecco's medium (Sigma-Aldrich) medium supplemented with Liberase-TL (100µgml−1, Roche) and DNase I (100µgml−1, Roche) at 37°C for 20min and dissociated with 18G and 21G needle. Blood was collected from the heart. Red cell lysis was performed on bone marrow and blood samples (RBC Lysis Buffer, Invitrogen). Isolated leukocytes stained cell surface markers for flow cytometry analysis and sorting. Cell populations were sorted using either SORP-aria (BD Biosciences) or ARIA-III instrument (BD Biosciences), and analyzed using BD FACSDIVA software (BD Biosciences) and FlowJo software.
Immune cells in Fig.1 were sorted as Cells -> singlets -> DAPI- ->CD45+
cDC in Extended data Fig.3a were sorted as Cells-> singlets -> ->CD45+ ->DAPI-Lin- ->MCH-IIhiCD11chi, cDC1 were gated as Cells-> singlets -> ->CD45+ ->DAPI-Lin- -> MCH-IIhiCD11chi -> CD103+XCR1+CD11b-, cDC2 were gated as Cells-> singlets -> ->CD45+ ->DAPI-Lin- -> MCH-IIhiCD11chi -> CD103-XCR1-CD11b+. mDC were gated as Cells-> singlets -> ->CD45+ ->DAPI-Lin- -> MCH-IIhiCD11chi -> CD86+/CCR7+
CDP (Fig.4, Extended data fig.6a) were selected as: cells -> singlets -> CD45+ -> Lin− -> CD135+CSF−1R+ -> CD117int -> BrdU+
preDC (Fig.4, Extended data fig.6a) were selected as: cells -> singlets -> CD45+ -> Lin− -> CD135+CD11c+ -> CD172- -> BrdU+
T cells (Fig 5, Extended data fig.7) were selected as: cells -> CD45+ -> Lin− -> CD11c-MHC-II- -> TCRb+
PICS (Fig 5, Extended data fig.7) were selected as: cells -> CD45+ -> Lin− -> CD11c+MHC-II+ -> TCRb+
CD8+ T cell subsets (Fig 6, Extended data fig.10) were selected as: cells -> singlets -> CD45+ -> Lin− -> CD11c+MHC-II+ -> CD8 + -> CD44+CD62L+(central memory)/ CD44+CD62L-(effector memory)/ CD44-CD62L+(naive)
CD4+ T cell subsets (Fig 6, Extended data fig.10) were selected as: cells -> singlets -> CD45+ -> Lin− -> CD11c+MHC-II+ -> CD4 + -> CD44+CD62L+(central memory)/ CD44+CD62L-(effector memory)/ CD44-CD62L+(naive)
Monocytes (Fig 6, Extended data fig.10) were selected as: cells -> singlets -> CD45+ -> CD11b+Ly6c+
NK (Fig 6, Extended data fig.10) were selected as: cells -> singlets -> CD45+ -> TCRb+-> NK1.1+

Peripheral blood from human patients was collected to EDTA-containing tubes (Becton Dickinson). Each sample was diluted 1:1 in ice cold FACS buffer. Mononuclear cell separation was performed by density centrifugation media (Ficoll-Paque; GE Healthcare Life Sciences) in a 1:1 ratio with diluted blood cells. Centrifugation (460g, 25min) was performed at 10°C, and the mononuclear cells were carefully aspirated and washed with ice-cold FACS buffer. After red blood cell lysis (Sigma-Aldrich) for 5min at 4°C and washing cells were frozen in 10% DMSO in FBS and stored at -80°C until further processing. On the day of the analysis, the cells were washed twice with FACS buffer, stained and analyzed using BD FACSDIVA software (BD Bioscience) and FlowJo software (FlowJo, LLC).
cDCs in human blood (Fig.3f-i, Extended data fig.5f) Cells -> single -> CD45+ -> Lin- -> CD11c+HLA-DR+. cDC1 were selected as CD1c-CD141+. cDC2 were selected as CD1c+CD141-.
Liver biopsies from bariatric surgery patients were collected in RPMI (Supplemented with 10%FBS) and immediately transported on ice to the laboratory. A section of tissue was formalin fixed for histopathological evaluation; however, the bulk of the tissue was digested using Miltenyi Tumor dissociation Kit (cat no. 130-095-929) as per the manufacturer's instructions. Single cell suspensions thus generated were stored in Liquid nitrogen in FBS+20% DMSO until further processing. For sorting and single cell RNAseq of DCs obtained from control and NASH livers, the stored cells were thawed in a 37oC water bath, washed once with complete media and once with FACS buffer (PBS+2% FBS). After FC blocking, cells were stained in dark for 30 min and washed once with FACS buffer and once with sorting buffer (PBS+0.5mM EDTA).
cDCs in human liver (Fig.3a,b, Extended data fig.6a) were gated Cells -> single -> live -> CD45+ -> Lin- -> CD11c+

Instrument

SORP-FACSAria or FACS-AriaIII sorter

Software

BD FACSDIVA V.9.0 software (BD Biosciences) and FlowJo software V.10.7.1.

Cell population abundance

scRNA-seq with index sorting was used to determine population purity in Fig.2,4,5,6. In fig 2,6, IHC was used to validate FACS data.

Gating strategy

Gating strategies for each FACS experiment are indicated in main and/or supplementary figures. Briefly:
Immune cells in Fig.1 were sorted as Cells -> singlets -> DAPI- ->CD45+
cDC in Extended data Fig.3a were sorted as Cells-> singlets -> ->CD45+ ->DAPI-Lin- ->MCH-IIhiCD11chi, cDC1 were gated as Cells-> singlets -> ->CD45+ ->DAPI-Lin- -> MCH-IIhiCD11chi -> CD103+XCR1+CD11b-, cDC2 were gated as Cells-> singlets -> ->CD45+ ->DAPI-Lin- -> MCH-IIhiCD11chi -> CD103-XCR1-CD11b+. mDC were gated as Cells-> singlets -> ->CD45+ ->DAPI-Lin- -> MCH-IIhiCD11chi -> CD86+/CCR7+
CDP (Fig.4, Extended data fig.6a) were selected as: cells -> singlets -> CD45+ -> Lin− -> CD135+CSF−1R+ -> CD117int -> BrdU+
preDC (Fig.4, Extended data fig.6a) were selected as: cells -> singlets -> CD45+ -> Lin− -> CD135+CD11c+ -> CD172- -> BrdU+
T cells (Fig 5, Extended data fig.7) were selected as: cells -> CD45+ -> Lin− -> CD11c-MHC-II- -> TCRb+
PICS (Fig 5, Extended data fig.7) were selected as: cells -> CD45+ -> Lin− -> CD11c+MHC-II+ -> TCRb+
CD8+ T cell subsets (Fig 6, Extended data fig.10) were selected as: cells -> singlets -> CD45+ -> Lin− -> CD11c+MHC-II+ -> CD8+ -> CD44+CD62L+(central memory)/ CD44+CD62L-(effector memory)/ CD44-CD62L+(naive)
CD4+ T cell subsets (Fig 6, Extended data fig.10) were selected as: cells -> singlets -> CD45+ -> Lin− -> CD11c+MHC-II+ -> CD4+ -> CD44+CD62L+(central memory)/ CD44+CD62L-(effector memory)/ CD44-CD62L+(naive)
Monocytes (Fig 6, Extended data fig.10) were selected as: cells -> singlets -> CD45+ -> CD11b+Ly6c+
NK (Fig 6, Extended data fig.10) were selected as: cells -> singlets -> CD45+ -> TCRb+-> NK1.1+
cDCs in human blood (Fig.3f-i, Extended data fig.5f) Cells -> single -> CD45+ -> Lin- -> CD11c+HLA-DR+. cDC1 were selected as CD1c-CD141+. cDC2 were selected as CD1c+CD141-.
cDCs in human liver (Fig.3a,b, Extended data fig.6a) were gated Cells -> single -> live -> CD45+ -> Lin- -> CD11c+

☒ Tick this box to confirm that a figure exemplifying the gating strategy is provided in the Supplementary Information.